Exploring Controlled Drug Release from Magneto Liposomes

by

George Podaru

B.S., Al. I. Cuza University, Iasi, Romania, 2009
M.S., Al. I. Cuza University, Iasi, Romania, 2011

AN ABSTRACT OF A DISSERTATION

submitted in partial fulfillment of the requirements for the degree

DOCTOR OF PHILOSOPHY

Department of Chemistry
College of Arts and Sciences

KANSAS STATE UNIVERSITY
Manhattan, Kansas

2017

Abstract

This thesis focuses on exploring fast and controlled drug release from several liposomal drug delivery systems including its underlying mechanics. In addition, the construction of a pulsed high-voltage rotating electromagnet is demonstrated based on a nested Helmholtz coil design. Although lots of different drug delivery mechanisms can be used, fast drug delivery is very important to utilize drug molecules that are short-lived under physiological conditions. Techniques that can release model molecules under physiological conditions could play an important role to discover the pharmacokinetics of short-lived substances in the body. In this thesis, an experimental method is developed for the fast release of the liposomes' payload without a significant increase in (local) temperatures. This goal is achieved by using short magnetic pulses to disrupt the lipid bilayer of liposomes loaded with magnetic nanoparticles.

This thesis also demonstrates that pulsed magnetic fields can generate ultrasound from colloidal superparamagnetic nanoparticles. Generating ultrasound remotely by means of magnetic fields is an important technological development to circumvent some of the drawbacks of the traditional means of ultrasound generation techniques. In this thesis, it is demonstrated that ultrasound is generated from colloidal superparamagnetic nanoparticles when exposed to pulsed and alternating magnetic fields. Furthermore, a comparison between inhomogeneous and homogeneous magnetic fields indicates that both homogeneous and inhomogeneous magnetic fields could be important for efficient ultrasound generation; however, the latter is more important for dilute colloidal dispersion of magnetic nanoparticles. In strong magnetic fields, the ultrasound generated from the colloidal magnetic nanoparticles shows reasonable agreement with the magnetostriction effect commonly observed for bulk ferromagnetic materials. At low magnetic fields, the colloidal magnetic nanoparticle dispersion produces considerable amount of

ultrasound when exposed to a.c. magnetic fields in the 20−5000 kHz frequency range. It is expected that the ultrasound generated from magnetic nanoparticles will have applications toward the acoustic induction of bioeffects in cells and manipulating the permeability of biological membranes.

Exploring Controlled Drug Release from Magneto Liposomes

by

George Podaru

B.S., Al. I. Cuza University, 2009
M.S., Al. I. Cuza University, 2011

A DISSERTATION

submitted in partial fulfillment of the requirements for the degree

DOCTOR OF PHILOSOPHY

Department of Chemistry
College of Arts and Sciences

KANSAS STATE UNIVERSITY
Manhattan, Kansas

2017

Approved by:

Major Professor
Viktor Chikan

Copyright

Abstract

This thesis focuses on exploring fast and controlled drug release from several liposomal drug delivery systems including its underlying mechanics. In addition, the construction of a pulsed high-voltage rotating electromagnet is demonstrated based on a nested Helmholtz coil design. Although lots of different drug delivery mechanisms can be used, fast drug delivery is very important to utilize drug molecules that are short-lived under physiological conditions. Techniques that can release model molecules under physiological conditions could play an important role to discover the pharmacokinetics of short-lived substances in the body. In this thesis, an experimental method is developed for the fast release of the liposomes' payload without a significant increase in (local) temperatures. This goal is achieved by using short magnetic pulses to disrupt the lipid bilayer of liposomes loaded with magnetic nanoparticles.

This thesis also demonstrates that pulsed magnetic fields can generate ultrasounds from colloidal superparamagnetic nanoparticles. Generating ultrasound remotely by means of magnetic fields is an important technological development to circumvent the drawbacks of the traditional means of ultrasound generation techniques. In this thesis, it is demonstrated that ultrasound is generated from colloidal superparamagnetic nanoparticles when exposed to pulsed and alternating magnetic fields. Furthermore, a comparison between inhomogeneous and homogeneous magnetic fields indicates that both homogeneous and inhomogeneous magnetic fields could be important for efficient ultrasound generation; however, the latter is more important for dilute colloidal dispersion of magnetic nanoparticles. In strong magnetic fields, the ultrasound generated from the colloidal magnetic nanoparticles shows reasonable agreement with the magnetostriction effect commonly observed for bulk ferromagnetic materials. At low magnetic fields, the colloidal magnetic nanoparticle dispersion produces considerable amount of

ultrasound when exposed to ac magnetic fields in the 20−5000 kHz frequency range. It is expected that the ultrasound generated from magnetic nanoparticles will have applications toward the acoustic induction of bioeffects in cells and manipulating the permeability of biological membranes.

Table of Contents

List of Figures

List of Tables

Acknowledgements

Dedication

I would like to dedicate this thesis to my father, Dumitru Podaru, for the strength and will to live, which he has shown to me daily, while fighting cancer. Also, I dedicate this thesis to my mother, Viorica Podaru, brother, Catalin Podaru and my girlfriend, Livia Cirnu for the continuous support offered throughout the years.

Chapter 1 - Introduction/rationale for drug delivery systems

1.1 Lipid-based drug delivery system

Lipids represent a broad class of chemicals which include phospholipids, fatty acids, glycerides, sphingolipids and sterols. In this class, there are also included all the derivatives and synthetic lipid analogs. Currently a wide range of lipids are available with a variety of physical and chemical properties. For example, lipids differentiate themselves by their fatty acid contents, melting point and solubility in organic solvents. Primarily lipids are dispersed in organic solvents due to their amphiphilic nature. In Figure 1 is shown the structural similarity of the lipid bilayer with the cell membrane, lipids representing a class of molecules which are well tolerated by living organisms.
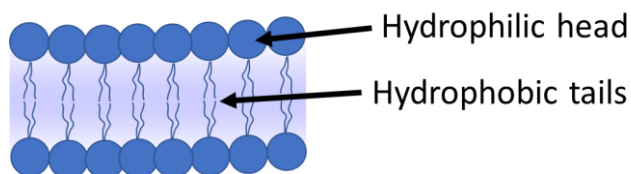
Figure 1 Bilayer formed from the arrangement of lipids

In their review, A. Khan[1] called the liposomes as "a lipid-based vesicular carrier systems" which can be easily altered in size, ranging from a 30 nm up to few microns. Formation of liposomes is relatively simple, and it only requires a dry film of lipids which is hydrated with an aqueous solution. Upon hydration, the lipid film will swallow and lipid vesicles will be formed. Due to its simplicity of formation, loading the liposomes with different molecules is straight forward. For example, Zhao et al.,[2] show a clinical trial in which a doxorubicin loaded

liposome system is used in treating breast cancer. These lipid-based formulations represent a great interest for encapsulation of different payloads. As described above, under certain conditions lipids will form liposomes, which consist of a bilayer of lipids arranged in a spherical form. As shown in Figure 2, liposomes can encapsulate both hydrophilic and hydrophobic drugs due to their structures.
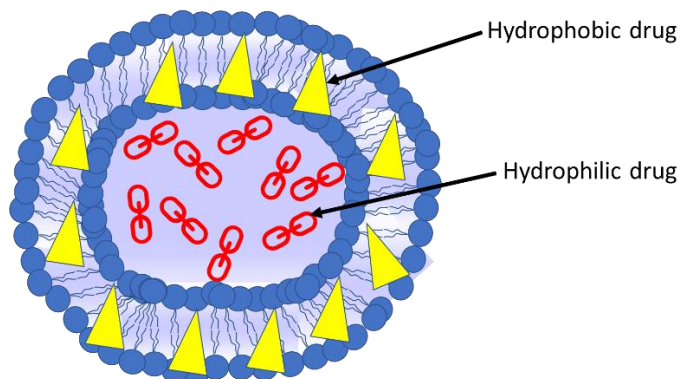
Figure 2 General scheme of liposomes encapsulating hydrophilic and hydrophobic drugs

The ability to transport and deliver throughout the entire biological system water insoluble or poorly soluble drugs, demonstrate that liposomes are a versatile drug delivery system. Liposomes can be classified based on their size and the number of bilayers they possess. Multilamellar (MLV) vesicles contain multiple concentric lipid bilayers while unilamellar vesicles (ULV) consist of an aqueous core surrounded by a single double layer of lipids. Furthermore, ULVs can be divided into large unilamellar vesicles (LUV) with a diameter ranging from 0.05 – 0.25 µm and small unilamellar vesicles (SUV) having a diameter of 0.05-0.10 µm.

The versatility of a drug delivery system arises from the ability that the liposomes can be modified and altered depending on the properties needed. For example, if one needs a good delivery system that can be used in the blood stream, its relatively easy to coat the liposomes

with polyethylene glycol (PEG) which will enhance the stability of the vesicles. Mahmud *et al.*,[3] showed that in the case of curcumin-loaded pegylated liposomes had a good stability up to 24 hours. In addition, they also presented another key aspect of the liposome carrier systems, which is the ability of carrying a highly insoluble molecule (curcumin) through the plasma.
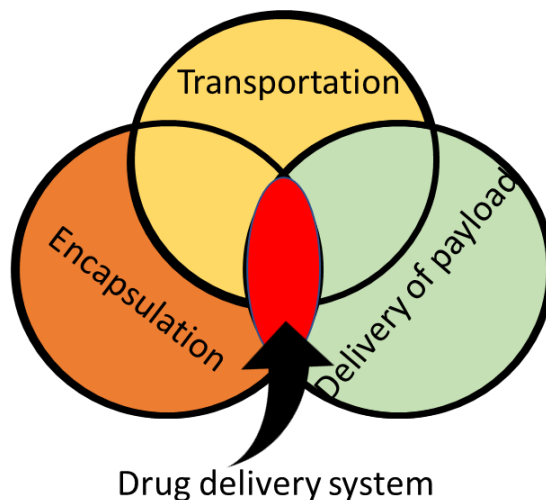
Figure 3 Diagram showing the requirement for an efficient drug delivery systems

A good drug delivery system, is characterized by its ability to encapsulate, transport, and deliver the payload to the target (Figure 3). In this regard, it is critical to discuss about the protection that liposomes offer to the payload. As stated before, the liposomes can encapsulate the payload either inside or into the lipid bilayer which is beneficial to the drug-medium interactions. Basically, until the release, there is no interaction between the payload and the surrounding medium because the lipid membrane protects the content. The lipid membrane is porous and it can be altered in different ways in order to change its characteristics. This is necessary for achieving a good protection of the payload, but also it needs to provide an accessible way to destroy the membrane for the purpose of delivering the drug. Different

methods and techniques of delivering the drug will be discussed in depth later, but first I will classify the liposomes based on their structure.

1.2 Common types of liposomes

Liposomes can be classified into numerous categories depending on the physical or chemical properties. Physical properties are characterized by size and number of bilayers while chemical properties refer to the types of lipids and the chemical alterations made to the lipid bilayer. There are numerous types of liposomes presented in the literature but for the purpose of this thesis, we will concentrate on the most common liposome used as a drug delivery system.

Conventional liposomes are prepared from phospholipids and cholesterol, but there is no additional protective outer layer or other ligands that will protect the surface of the liposome. Cholesterol is added to the mix of lipids in order to strengthen the lipid membrane. The charge of these liposome will depend strictly on the lipids used when prepared. The encapsulation of the payload is in the interior space of the vesicle, and they were first used to encapsulate doxorubicin that targeted the reticuloendothelial system[1]. In that study, it has been shown that the liposomes were able to reduce the circulation time and also prolonged the drug distribution compared to conventional systems.

Ethosomes are liposomes that consist of a hydro-alcoholic core. The unique property of the ethosomes is represented by the fact that they can penetrate the skin layer[1]. Due to the alcoholic reservoir that is found in the core of the liposome, they have an increased fluidity and stability which increase the ability to penetrate and induce transdermal delivery of the drug by enhancing the depth of penetration, distribution and deposition of the payload[4].

Novasomes represent another type of liposome, formed from polyoxyethylene fatty acids monoesters, free fatty acids and cholesterol[1] ranging from 100 nm up to 1000nm. The distinguished property of these liposomes is that they can encapsulate simultaneously hydrophilic and hydrophobic payloads. Novasomes consist of multiple bilayers (up to seven) and they can incorporate a large amount of drugs.

Virosomes are a modified form of the regular liposomes in which the exterior surface is modified with fusogenic viral envelope proteins[1]. These liposomes are used for delivering antigens and anti-cancer drugs, however they are prone to low stability and leakage. First virosomes were designed to deliver DNA intracellulary while later they were loaded with a vaccine.

Stealth liposomes also called immune-liposomes, are prepared with polyethylene glycol lipids. Just like the name suggests, the stealth liposomes, have the ability to "hide" from the immune-response of the bio-system. Unlike conventional liposomes, they have a much higher survivability rate (half life equals to 24 hours) and with the use of outside bond ligands they can reach a specific target.

pH sensitive liposomes have been designed to deliver the payload in an environment that can be manipulated through pH changes. For example, the liposomes are stable at physiological pH but the payload is released when they encounter an acidic medium.

Magneto-liposomes are constituted from a blend of conventional liposomes and a ferromagnetic/superparamagnetic material and they release the payload or be site-directed under the action of a magnetic field.

The advantages and constituents of new generation liposomes are summarized in Table 1-1.

Type of liposomes	Constituent	Advantage of liposomes
Conventional liposomes	Phospholipids	
Emulsomes	Phospholipids with a solid fat core	High loading of hydrophobic drugs
Ethosomes	Alcohol and Phospholipids	Good transdermal penetration
Genosomes	Cationic phospholipids with a functional DNA or gene	Gene/DNA delivery
Magneto-liposomes	Phospholipids blended with ferromagnetic nanoparticles	Effective targeting, in depth delivery
Novasomes	polyoxyethylene fatty acids monoesters, free fatty acids and cholesterol	High encapsulation of drugs
pH sensitive liposomes	dioleoylphosphatidylethanolamine	Effective targeting, long circulation in plasma
Stealth liposomes	Lipids modified with polyethylene glycol	Enhanced biological stability
Virosomes	Lipids modified with fusogenic viral envelopeproteins	Intracellular delivery of DNA and anti-cancer drugs

Table 1-1 Summary of new generation liposomes

Liposomes should be characterized after preparation to be certain that all required

properties are met when exposing them to the in vitro and in vivo medium. There are a few key

features that need to be confirmed before performing an experiment: diameter, size distribution, number of bilayers, concentration, and encapsulation efficiency of the payload. The most common technique to determine the size of the liposome is dynamic light scattering which ensures a rapid and simple way to measure the average size of the liposome bulk. If an accurate characterization of the liposomes is necessary, one can use the electron microscopy due to the possibility of observing individual liposome, and precisely obtaining information about the population of liposomes in the whole sample. To prevent the liposomes from fusing, its common to measure the electronic stabilization i.e. surface charge, by zeta potential measurements. It is essential to measure the amount of the material encapsulated in the liposome, Buboltz *et al.*,[5] showed that typically, this is obtained by the destruction of the lipid bilayer (100% release) and quantifying the released material.

For the liposomes to be used in the pharmaceutical industry, they must be sterilized. Common methods of sterilization include the terminal sterilization of the final product (steam sterilization) or aseptical manufacturing of the liposomes.[4] Terminal sterilization is preferred due to a higher assurance level of sterility compared to aseptical sterilization procedures. Due to the susceptibility of liposomes to physical and chemical degradation, it is challenging to find a convenient method of sterilization. Several procedures for sterilization of liposomes are filtration, dry heat sterilization, gamma irradiation, steam sterilization, ethylene oxide sterilization or ultraviolet sterilization.[4] The most effective and common method for sterilization of liposomes is filtration due to the fact the no heat is used, therefore the liposomes are not subjected to heat degradation or leakage. A drawback of sterilization of liposomes through filtration is that the method needs to be performed under aseptic conditions. It is time consuming and needs to be performed to the liposomes that are 200 nm or smaller.

1.3 State of the art of lipid-based drug delivery systems

In the recent years of biomedical research, the need for a versatile and effective drug delivery platform has increased due to the challenges that diseases like cancer or malaria poses. The use of nanotechnology in drug delivery systems has become irreplaceable as the advancement in the pharmaceutical industry thrived. Initially, one clear direction for developing a better drug delivery system has been approached: the achievement of an improved fractional distribution of the payload at the targeted site.[6] With the introduction of lipid-based drug delivery systems a void has been filled in this field. As lipid-based delivery systems have been effective at enhancing the efficacy of the chemotherapeutic agents for cancer treatments,[7] novel drug delivery platforms are currently being investigated.

Magnetic Liposomes. The term of magnetic liposomes refers to the fact that magnetic nanoparticles (magnetite, maghemite) and the drug, are encapsulated within the liposome. With the help of a magnetic field this drug delivery technique can be targeted into the tumor. The liposomes are administrated intravenously and with the help of a carefully placed magnetic field the liposomes can be concentrated at the tumor site.[8] The typical size of the encapsulated magnetic nanoparticles is less than 10 nm. Nabuto et al.,[8] showed a study, where magnetic liposomes encapsulated with doxorubicin have been intravenously administered to a hamster with a limb osteosarcoma. The limb was placed in a magnetic field (0.4 T) and after 60 minutes, the concentration of doxorubicin at the tumor site was increased by a factor of 4.

Redox sensitive liposomes. A high reduction potential difference is present close to the cell membrane due to increased number of reducing agents such as glutathione.[9] The difference in the reduction potential between the extracellular and intracellular mediums should, and can be

exploited with the help of redox-sensitive liposomes. To reach the target, liposomes can be coated with a ligand conjugated by disulfide bond. The disulfide bond will be destabilized by the glutathione when the liposomes enter the intracellular compartment of the cell, thus, the payload will be released from the liposome.

Ultrasound sensitive liposomes. In 2015, the development of echogenic (the ability to reflect ultrasound waves) liposomes[10] allows the payload to be released via ultrasounds. These liposomes contain an emulsion that is vaporizable that results in a high response from the ultrasounds. Javadi *et al.*,[11] showed that eLiposomes, liposomes that have an liquid emulsion of perfluorocarbons encapsulated, are ruptured by decreasing the local pressure below the vapor pressure of the emulsion. The change in pressure makes the perfluorocarbon emulsion to vaporize and the liposomes become sensitive to ultrasounds.

Enzyme sensitive liposomes. Several enzymes have been found to be overexpressed at the tumor site like phospholipase A_2, transglutaminase, alkaline phosphatase or matrix metalloproteinases[12] To exploit this enzyme overexpression, liposomes can be engineered with a linker that will be cleavable in the presence of these enzymes. Upon the cleavage of the linker the surface of the liposomes will be altered for a better adhesion to the cell membrane. In 2012, Zhu *et al.*,[13] presented a system in which a drug delivery method was developed in response to the up-regulated matrix metalloprotease 2 (MMP2). The surface of the liposome was functionalized with a polyethylene glycol lipid conjugate, and upon reaching the cell membrane, the lipid conjugate was cleaved by the MMP2, exposing a cell penetrating peptide which enhanced intracellular delivery.

Liposomes for photodynamic therapy. Photodynamic therapy is a treatment that uses the response of a photosensitizing agent upon exposing it, to a certain wavelength of the light. Upon

exposure to the light the photosensitizer will generate reactive oxygen species that will kill the cancer cells.[14] In this type of delivery system, the liposome's role is to protect the photosensitizer from aggregation, improve the concentration, reduced phototoxicity and to improve target specificity. This type of therapy is used for treatment of superficial tumors.

1.4 Combination of nanoparticles and liposomes for drug delivery

Cancer is a leading cause of worldwide death and in order to beat it, researchers have developed various strategies, starting with surgery, chemotherapy, radiotherapy, hyperthermia, targeted therapy, and even hormone therapy.[15] Chemotherapy represents the last resort in fighting cancer, but due to the lack of specificity and toxic side effects scientists searched for an alternative method to deliver drugs to the tumor site. In chemotherapy, anticancer drug is intravenously or orally administrated to the patient. Thus, the dug is systemically circulated throughout the body without a special localization to cancer site.[16] Nanomedicine represents a new direction that has been approached in order to solve the drawbacks of current therapies. Implementation of nanotechnology in cancer treatment must provide novel therapeutics while reducing the side effects of anticancer drugs to healthy cells. Nanotechnology can improve current treatments by the application of different nanovectors such as lipid-based structures, dendrimers, several metal nanoparticles, polymers and polymer-drug conjugates.[15] The term of nanovectors refers to nano-scale drug delivery systems. Along with several drug delivery systems, liposomes present a great interest in the field of drug delivery. A schematic of nanoparticle-liposome drug delivery system is presented in Figure 4. First, the nanoparticles and drugs are encapsulated into liposomes (synthesis), following by the liposomes injection into the blood stream (transportation). Finally,

upon exposure to a nanoparticle sensitive technique, the drug is release at the tumor site (delivery).
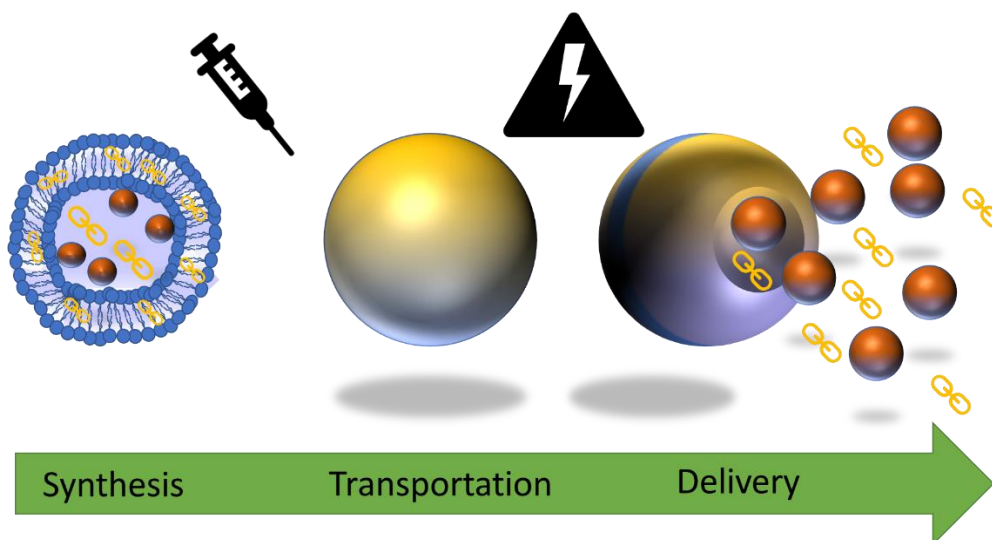
Figure 4 Schematics of a nanoparticle-liposome drug delivery system

In his dissertation, Matthew Basel, describes two methods for targeting a cancerous tumor with the help of a drug delivery system based on liposomes that are sensitive to cancer associated proteases.[17] In comparison to other drug delivery systems, liposomes allow the encapsulation of both hydrophilic and hydrophobic drugs, good biocompatibility, capacity for self-assembly and protect the payload from external environment.[18] On the other hand, metallic nanoparticles have been successfully used in cancer therapies.[19] For example, Zhang *et al*.,[20] showed that ultra-small gold nanoparticles (2.7 nm) doxorubicin conjugated, enter in the endocytic vesicles of B16 melanoma cells, resulting in a 20-fold increased toxicity compared to the equivalent concentration of doxorubicin. Nanoparticles can improve drug delivery to cancerous tumors without the need of localized or specific targeting. Such a phenomena is caused by the enhanced penetration and retention (EPR) effect, due to the enhancement of extravasation at the tumor site.[21] Extravasation refers to the leakage of intravenously injected

drugs into the extravascular tissue around the tumor site. Other examples of metallic

nanoparticles used in drug delivery systems are:

- Neodymium based ultrasmall nanoparticles – used in photothermal therapy[22]

- Copper ferrite – used in studies for reducing the viability and damaging the membrane of MCF-7 cells (human breast cancer cells)[23]

A combinational drug delivery system formed from metallic nanoparticles and liposomes might improve the efficacity of the drug delivery system or enhance a fast release of the payload. It is possible to combine the liposomes with metallic nanoparticles to improve drug delivery systems even further. Several studies have shown that a liposome based drug co-delivery systems improve drug's pharmacokinetics and therapeutic effects while decreasing its adverse side effects.[15]

1.5 Means of actuation of liposome based drug delivery systems

Application of nanotechnology for the treatment of cancer or other diseases has led to the development of several drug delivery systems based on different technologies.[24] Since the introduction of liposomes in drug delivery platforms, scientist have searched a way to improve the efficacity and active drug targeting of liposomal based delivery systems.[25] In this chapter, we will discuss the advantages and drawbacks of the latest state of the art delivery systems.

1.5.1 Enzyme activated drug delivery

Understanding the tumor specific microenvironment changes or variations from the healthy cells, represents the key to a specific and targeted drug delivery system. For this purpose, several

enzyme activated systems have been developed with a simple aim: to take advantage of the changes that occur in the surrounding microenvironment of the tumorous site. Phospholipase A_2 ($sPLA_2$) is a secretory enzyme that is overexpressed in tumors. The role of PLA_2 enzymes in the human body is to downregulate cell signals via the cleavage "deactivation" of bioactive phospholipids.[25] A subtype of PLA_2 enzymes, $sPLA_2$ IIA, is suspected to have a role in tumorigenesis and metastasis and it is overexpressed in several cancer types, like prostate, breast and colon cancer.[26] Patients suffering from lung or gastric cancer have an elevated level of $sPLA_2$ enzymes of 28% while for patients with liver cancer the percentage increases to 100%.[27]

Utilizing the elevated levels of $sPLA_2$ at the tumor site as a trigger for a drug delivery platform can lead to a specific and targeted treatment. Liposomes containing anticancer drugs and that were susceptible to $sPLA_2$ have been developed,[25] and the release was precisely triggered by the enzyme. Andresen et al.,[28] have analyzed various $sPLA_2$ degradable liposomes, with different lipid composition (DSPC/DSPG/DSPE-PEG2000) loaded with doxorubicin. After 5 hours of incubation in a media containing $sPLA_2$ secreted from colon cancer cells, they found the release of doxorubicin to be 80%.

1.5.2 Light activated drug delivery

Light can be used as a triggering method for a drug delivery system due to a high spatial and temporal control. The penetration depth of light is largest in the near IR region. Beam diameter, intensity and the wavelength of light, can be easily modified to create a unique and versatile method for triggering drug release.[29] Up to date, several light triggering techniques have been developed depending of the type of light used. For example, ultraviolet light is used in

isomerization, polymerization, photocleavage or conversion of energy to heat. Visible light is used in polymerization, oxidation or energy conversion to heat, while near-infrared light is mostly used for the conversion of energy to heat.[29] Light activated drug delivery systems can be used in two different ways, the delivery system can have a "single use" (the payload is fully released upon triggering) or the platform can be switchable (the payload can be switched on and off for a stepwise release).[30] The whole concept of using light to trigger the release of the liposomes' payload, is based on the fact that light will introduce a structural change in the system that will lead to the drug release.

Lajunen *et al.*,[29] describe a drug delivery system formed from indocyanine green (ICG) loaded liposomes and ARPE-19 cells (human retina cells). The internalization of ICG liposomes (100 nm) into ARPE-19 cell line was investigated through flow cytometry. Calcein loaded ICG liposomes were successfully internalized by the cells and upon exposure to near-infrared light (9.7 W/cm^2, 2 min) calcein was released into the cells. The fluorescence of the cells showed a 2-3-fold increase compared to the control sample (sample was not exposed to near-infrared light). There are two possible mechanisms for the release of calcein: 1) exposure to light increases the temperature and causes leakage in the liposomal wall; 2) the increase in temperature forced the fusion of the liposomal membrane with the vesicular walls leading to the delivery of the payload into the cytosol.

Although there are several studies showing drug release via light activation of liposomes in vitro,[31] it is important to say that light activation drug delivery is not a viable method for obtaining drug release from liposomes in vivo, because of the limited transmission of the light through the body. The method needs to be significantly developed before it can be a successfully drug delivery platform.

1.5.3 "Traditional" focused ultrasound delivery

Ultrasound consist of longitudinal pressure waves that propagate through a medium with a frequency higher than the audible ones for the human ear, i.e. higher than 20kHz.[32] Ultrasound waves can be classified depending on the frequency as low frequency, (20-200 kHz) medium frequency. (0.6-3 MHz) and high frequency (>3MHz).[33] In medicine, ultrasound is generated using piezoelectric transducers, which convert a high frequency alternating current into acoustic vibrations.[34] Several criteria must be taken into account when choosing the ultrasound frequency: penetration depth (frequency of the ultrasound wave is invers proportional to penetration depth; 1MHz – 10 cm) and the spatial resolution (frequency of the ultrasound wave is direct proportional to spatial resolution; used mostly for imaging). Focused ultrasound waves allow the deposition of a high energy into a small zone of the body, (usually the size of a rice grain) while unfocused ultrasound is used to insonify large tumors.[32]

In the recent years, drug delivery systems have been developed to take advantage of the fact that ultrasounds are known to induce biological effects like thermal effects, mechanical effects and radiation forces.[32] Several studies showed that ultrasounds enhanced the uptake of drugs in cells and tissues by compromising the integrity of cell membranes (sonoporation).[33] Ultrasound have been also used in liposomal systems with encapsulated drugs, in which the release was triggered by the ultrasound at the site of interest.[35]

In their study, Myhr *et al.,*[36] analyzed the effects of low frequency (20 kHz) ultrasound exposure of liposome (doxorubicin encapsulated) on 144 Balb/c nude mice inoculated with WiDr (human colon cancer) cell lines. The results are encouraging, showing for the first time that upon exposure to non-hyperthermic ultrasounds, liposomes with encapsulated cytostatic drugs

significantly hindered tumor growth. Furthermore, they showed that the synergetic effect

between the ultrasounds and drugs was larger in the cases where low drug concentration was

used. Thus, patients for whom chemotherapeutic treatment has a minimal effect may benefit

from this type of treatment.

However, the "traditional" ultrasound therapy can be challenging due to attenuation as

ultrasound travels through bones, soft tissue or air.

1.5.4 Magnetic drug delivery

As previously discussed, the synergistic effect of co-delivery therapies can enhance the efficacity

of a drug delivery system, therefore getting closer to defeat cancer. Beside the techniques

previously presented in this thesis, magnetic drug delivery has been used to improve the

drawbacks of current delivery systems. Magnetic drug delivery refers to a system which is

composed of a magnetic field susceptible material and the application of the magnetic field as a

trigger for drug release. For the treatment of cancer or infectious diseases it is desirable to deliver

the payload at once after the target has been reached.

To satisfy the need for a fast and localized delivery, a new delivery system has been

developed, magneto-liposomes. Magneto-liposomes are a co-delivery system formed from the

combination of a metallic nanoparticle (e.g. iron oxide) and liposome. The magnetic

nanoparticles with a diameter that is larger than 10 nm are encapsulated into the aqueous core of

the liposomes, while nanoparticles with diameter smaller than 5 nm can be entrapped into the

bilayer of the liposome. Furthermore, the magnetic nanoparticles surface needs to be

appropriately prepared depending on the localization. For example, nanoparticles incorporated in

the aqueous core of the liposome need to be hydrophilic, while for the incorporation in the lipid bilayer, they need to be hydrophobic for compatibility purposes with the liposomes.

Several liposomal drug delivery systems have been developed[37] that rely on the slow release of their payload. However, fast drug delivery is very important to utilize drug molecules that are short-lived under physiological conditions. Currently, for magneto-liposomes systems, there are two main mechanistic methods of delivering the drug: AC magnetic hyperthermia[38] and a pulsed application of the magnetic field.[39] The mechanism of hyperthermia is dependent of selective tumoral cell heating (41-46 °C) leading to cell apoptosis. Several research groups[38] have used AC magnetic hyperthermia to trigger the release of magneto-liposomes' payload by heating magnetic nanoparticles within the supramolecular nanostructure until either burst or (partially) dissolve in the surrounding aqueous medium. Although this approach appears to work, it has the disadvantage that the liposomes' payload may be damaged by the head and the release is not instantaneous. This is certainly valid for anticancer drugs like SN-38 and its prodrug irinotecan[40] and si-RNA[40b] that can degenerate when heated above 56 °C. Another downside to be considered in the mentioned systems, refers to the fact that the release of drugs takes place on a minute time scale.
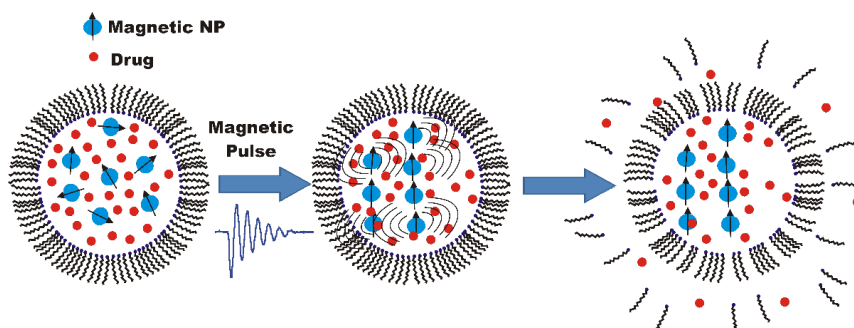
Figure 5 Illustration of a typical pulsed magnetic field inducing drug release from magneto-liposome. Reprinted with permission from ref.[39] Copyright (2014) American Chemical Society

The versatility of magneto-liposomes systems arises from the method that is used to deliver the payload. As stated previously, AC magnetic hyperthermia has been successfully used in cancer treatments but with some drawbacks (i.e. slow release of the drug, drugs can be damaged by heat). To eliminate the drawbacks of AC magnetic hyperthermia, a new method, presented in Figure 5, has been developed, pulsed magnetic field drug release. The method is developed for immediate release of the liposomes' payload without a significant increase in the local temperature. This goal is achieved by using the mechanical motion of the magnetic nanoparticles that are embedded within either the cores of the lipid bilayers of the liposomes, or at the interface between core and bilayer. The application of a strong magnetic pulse induces the mechanical motion of the magnetic nanoparticles and locally destabilizes the lipid bilayer and causes its collapse, subsequently releasing the liposomes payload. In contrast to the head-induced release from magneto-liposomes from AC magnetic fields, the drug release takes place due to mechanical motion of magnetic nanoparticles, therefore producing a significantly smaller amount of residual heating.

1.5.5 Thesis contributions

Advancements in nanotechnology lead to nanomedicine, that improved the overall cancer survival rate because of combinational therapies. The overarching goal of this work, aims at providing alternative drug delivery methodology in order to address the shortcomings of existing drug delivery systems based on liposomes. Pursuing this goal, I wanted to focus on the following aspects of liposomal drug delivery systems in this dissertation:

(1) I will demonstrate the synthesis of liposomes loaded with superparamagnetic nanoparticles and model drug molecules (Chapter 2).

(2) I will present data on building and characterizing electromagnetic coils for the generation of strong magnetic fields that can be in liposomal drug delivery (Chapter 2).

(3) I will show the construction of a pulsed high-voltage rotating electromagnet based on a nested Helmholtz coil design, for future use of drug release studies (Chapter 3).

(4) I will prove and attain fast and controlled drug release from magneto liposomes upon exposure to various magnetic fields (Chapter 4).

(5) I will investigate and clarify ultrasound generation from colloidal iron oxide nanoparticles upon exposure to homogeneous and inhomogeneous magnetic fields (Chapter 5).

Chapter 2 - Experimental tools and synthesis techniques

2.1 General approach to synthesize unilamellar liposomes

Liposomes are produced by the thin-film hydration method coupled with sequential
extrusion method which is adopted from the Ph.D. thesis of Matthew T. Basel.[17] To prepare
magneto liposomes (Figure 6), 88:1:10 molar ratio of 1,2-dipalmitoyl-sn-glycero-3-
phosphocholine (DPPC), 1,2-distearoyl-sn-glycero-3-phosphocholine (DSPC), and cholesterol
are mixed for total lipid of 10 mg in a round-bottom flask. Then, in order to ensure a
homogeneous mixture of the lipids, purchased powdered lipids are dissolved in an organic
solvent (chloroform).
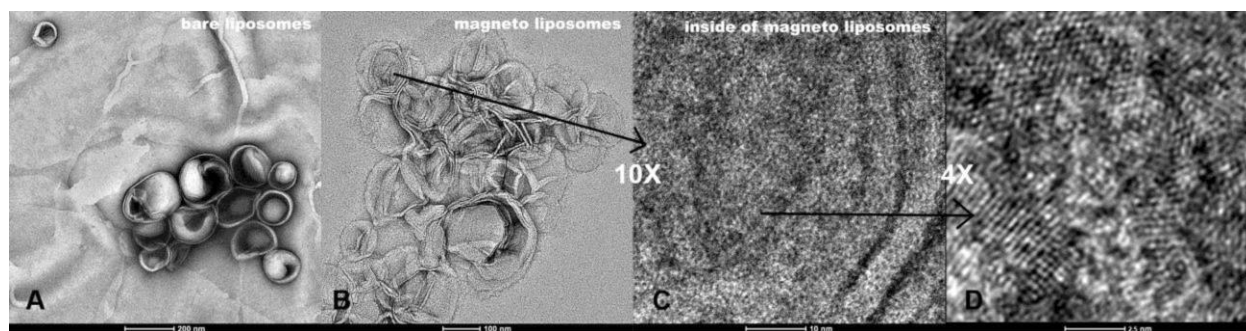
**Figure 6 (A) TEM image of bare liposomes. (B) TEM image of magneto liposomes. (C)
TEM image of inside a magneto liposome of image B showing the PtFe nanoparticles. (D)
HRTEM image of the PtFe nanoparticles from image C. Reprinted with permission from
ref.[39] Copyright (2014) American Chemical Society**

The solution was then vortexed for 1 min to ensure the even dispersion of the lipids and
cholesterol. DSPC and DPPC are the phospholipids used to create the lipid bilayer of the
liposomes, and cholesterol is added for increased stability. Once these compounds have been

added, the chloroform is evaporated off at approximately 55 °C. After evaporating the chloroform, the sample is placed in vacuum for 1 h. The next step is hydration of the thin-film lipid which is carried out simply by adding and agitating an aqueous medium into the thin-film of the lipids. Next, the residue is hydrolyzed to which either 125 µL of phosphate buffered saline (0.136 M NaCl, 0.0045 M KCl, 0.012 M phosphate- buffered to pH 7.4) or 125 µL of HEPES buffered saline (0.136 M NaCl, 0.0045 M KCl, 0.012 M HEPES buffered to pH 7.4), together with 838 µL of double distilled water and 37 µL of 3 M NaOH are added to the dried phospholipids. During this step, the encapsulation of a defined amount of nanoparticle solution (FePt or Fe/Fe$_3$O$_4$), MgSO$_4$ (25 mg), and carboxyfluorescein (25 mg) occurs simply by adding the desired amount to the lipid solution. If the nanoparticles are insoluble in water, one should mix them with lipid before making the thin film of lipid.

For control experiments, the same protocol was used, the only difference being the fact that no nanoparticles were added. After everything has been added to the lipid/nanoparticle solution, the mixture is vortexed for a minimum of 5 min. This creates the multilamellar liposomes which are larger than the final desired product (unilamellar liposomes). The next step is the freeze/thaw process. The mixture is placed in dry ice for 5 min and then placed in a 50 °C water bath for 5 min. This procedure is repeated 10 times. At the end of the process, the solution stays in the hot water bath. Next is the extrusion process where the multilamellar liposomes become the desired unilamellar liposomes, typically 50−250 nm in diameter. The solution is kept at 50 °C and extruded through a 200 nm pore diameter filter 11 times, ending on the opposite side from where the liposomes began. The final step is gel filtration in which the unilamellar end product is isolated from anything else present in the solution. The separation column is filled with a slurry of sephadex and phosphate buffered saline solution. The magneto liposomes are

collected in the first fraction from the column during the final separation step. The collected fraction of the magneto liposomes is analyzed via dynamic light scatterring resulting in a diameter of 200 nm ±30 nm.

.

2.2 Fluorescence based permeability measurements of liposomes

To investigate the permeability of magneto liposomes upon exposure to the magnetic field, a drug model molecule 5(6)-carboxyfluorescein (CF), is encapsulated into the liposome. The model drug of the investigation, CF, is responsible for the fluorescence emission from thus prepared liposomes. CF is a hydrophilic fluorescent molecule and it should be entrapped in the core of liposome. CF generates emission fluorescence at around 517 nm. The intensity of CF fluorescence gives the amount of free CF in the system. The change in fluorescence intensity is measured upon exposure to the pulsed magnetic field. The fluorescence self-quenching decreases as the CF molecules come out from the liposomes.[41] The steady state fluorescence is measured at excitation wavelength 460 nm with 1 nm slits. To calculate the drug release from both control liposomes and magneto liposomes, 200 µL of thus prepared liposomes or magneto liposome is diluted using 3 mL of PBS buffer. The emission fluorescence spectra of liposomes before exposing into pulsed magnetic field, after exposing into 10 pulses of pulsed magnetic field, and after the addition of 100 µL of Triton X-100 are recorded. The addition of Triton X-100 completely releases the CF through vesicle disruption.

2.3 AC conductivity based permeability measurements of liposomes

AC measurements are conducted with a potentiostat capable of conducting AC impedance measurements. The electrodes are commercially available carbon-printed electrodes, using three electrode configurations. As a first test, the conductivity of $MgSO_4$ is tested for different concentrations (Figure 7). Frequency in hertz is displayed on the x-axis, and the amplitude of the impedance in ohms is displayed on the y-axis. Impedance is the measure of the maximum volts across the circuit divided by the total current across the circuit, and it is inversely proportional to conductivity. Therefore, the lowest concentrations have the highest impedance values because they are the least conductive.
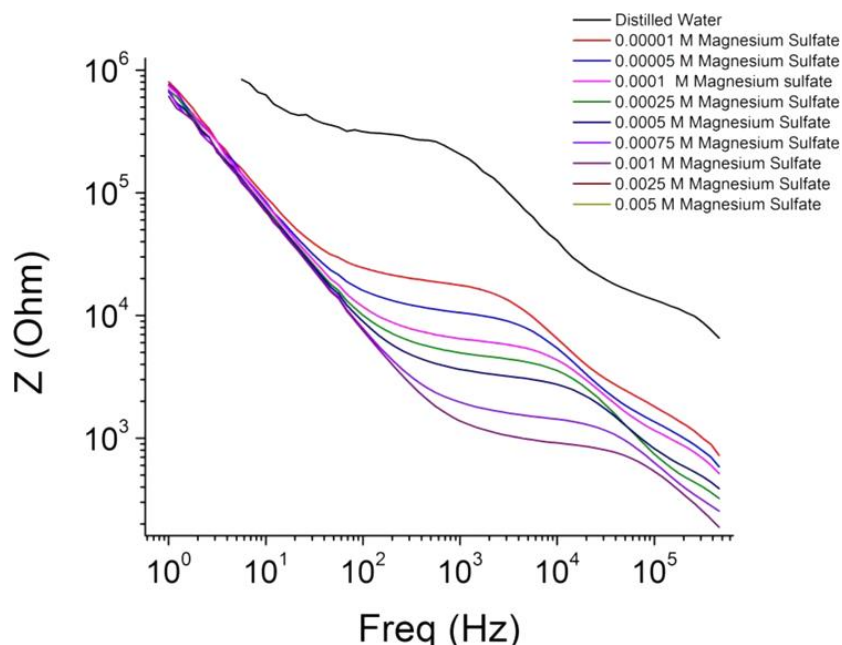
Figure 7 Bode plot of magnesium sulfate at different concentrations. Reprinted with permission from ref.[39] Copyright (2014) American Chemical Society

The black line represents distilled water which ideally would not have any ions at all. The red line is the lowest concentration of $MgSO_4$. It is only 1.0×10^{-5} M, yet there is a significant difference between the impedances of the distilled water and the 1.0×10^{-5} M $MgSO_4$. This demonstrates how sensitive impedance spectroscopy is to low concentrations of ions. As the concentration of $MgSO_4$ is increased, a decrease in impedance or an increase in conductivity, is observed.

2.4 Synthesis of Magnetic Nanoparticles

PtFe nanoparticles (Figure 8), are synthesized via the following procedure described by Chao Wang et al.[42] Into a three-neck round-bottom flask are loaded 0.015 mol of oleylamine and 0.015 mol of octadecene and 0.00025 mol of platinum(II)acetylacetonate ($Pt(acac)_2$). This flask is purged, vacuumed, and backfilled with argon gas three times, and the temperature is raised to 60 °C. The solution is allowed to sit there for 10 min and then quickly heated (in less than 5 min) to 120 °C. Upon reaching 120 °C, 0.00025 mol of iron pentacarbonyl is rapidly injected into the flask and the temperature raised to 160 °C and allowed to sit at this temperature for 30 min. Particles are then allowed to cool to room temperature and were cleaned using standard centrifugation (rinse 3 times hexane/ethanol) and redissolved in hexane.
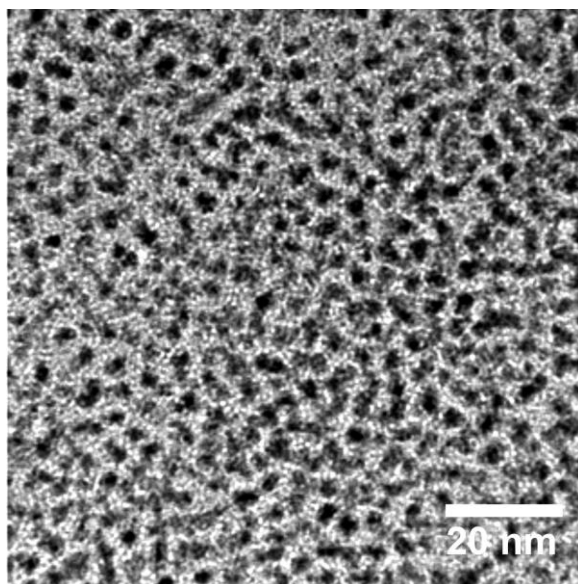
Figure 8 FePt nanoparticles synthesized by Chao Wang protocol[42]. Reprinted with permission from ref.[39] Copyright (2014) American Chemical Society

Iron nanoparticles are prepared with slight modification of a literature procedure described by Lacroix *et al.*[43] A 250 mL, three-necked, round-bottom flask equipped with a magnetic stir bar, one cold water cooled jacket condenser on the middle neck and one septum and one temperature probe on each of the outer necks is charged with 60 mL 1-octadecene (ODE), 0.9 mL oleylamine, and 0.831 g hexadecylammonium chloride (HAD·HCl). The reaction system is connected to a Schlenk line through the top of the jacket condenser. The reaction mixture is degassed at 120 °C for 30 min with vigorous stirring. After refilled with argon, the reaction mixture is heated to 180°C. Three portions of 0.7 mL $Fe(CO)_5$ are injected into the reaction mixture via a syringe every 20 min. The reaction mixture is kept at 180 °C for another 20 min after the last injection and cooled to room temperature naturally. The supernatant is decanted, and the iron nanoparticles accumulated on the magnetic stir bar are washed with hexane and ethanol. The product is dried in vacuum and stored at room temperature for further

use. Based on iron, the yield of the reaction is 95%. Three coatings of Fe/Fe_3O_4 will be used by attaching either hydrophilic, amphiphilic, or hydrophobic peptide sequences. HIV-1 Tat-(48−60) (GRKKRRQRRRPPQ) will serve as the hydrophilic oligopeptide. In its monomeric form, it is known to bind to double-layers. Penetratin will be employed as the amphiphilic oligopeptide (RQIKIWFQNRRMKWKK), and membrane translocating sequence peptide (AAVALLPAVLLALLP) will be used as the hydrophobic oligopeptide.

Core/shell magnetic Fe/Fe_3O_4 nanoparticles were first coated with dopamine, through which free NH_2 groups were introduced into the surface of nanoparticles (Figure 9). Next, reacting the C-terminal of hydrophilic, amphiphilic, or hydrophobic peptide sequences with the NH_2 groups resulted in the peptide functionalized magnetic nanoparticles.
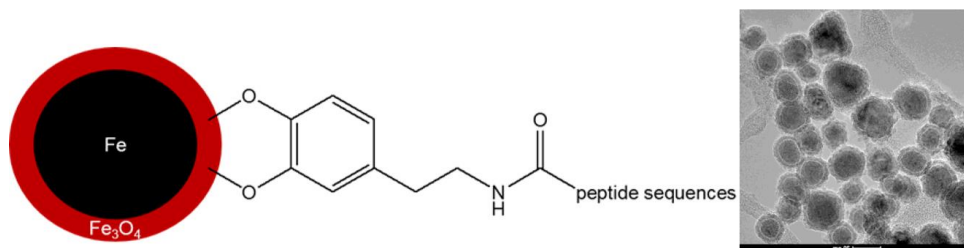
Figure 9 (Left) Schematic view of the iron oxide nanoparticles coatings for the release studies presented in this thesis. The peptide sequence modification allows modifying the hydrophobicity of the nanoparticle coating. (Right) TEM image of core/shell magnetic Fe/Fe_3O_4 nanoparticles. Reprinted with permission from ref.[39] Copyright (2014) American Chemical Society

Briefly, 10 mg of dopamine-coated Fe/Fe_3O_4 nanoparticles were dispersed into 2 mL of dry DMF, 5 mg of peptide sequence, 0.6 mg of EDC, 0.3 mg of DMAP were added to the suspension sequentially. After brief sonication, the reaction mixture was swirled vigorously at room temperature for 12 h. Magnetic nanoparticles were collected by centrifugation (10000 rpm, 5 min), and washed with DMF (2 mL × 3 times) and methanol (2 mL × 3 times). The

nanoparticles were finally dried under vacuum and stored under argon for liposome loading. The commercial 10 nm iron oxide nanoparticles used in the ultrasound studies were purchased from Ferrotec EMG series, and they are water-based ferrofluid type EMG 607 stabilized with cationic surfactant.

2.5 Construction of pulsed electromagnet for drug release studies

In 1924, the first pulsed magnetic field, close to 50 T, was developed by P. Kapitza from his lead acid storage battery through 1 mm bore, and he was optimistic about obtaining 200−300 T if adequate financial means became available.[44] Pulsed magnets are used for two reasons: they can provide the highest fields and they can be made to fit a moderate budget. The generation of pulsed magnetic field is important for several activities in the area of physical sciences. The basic components of a pulsed magnetic field are capacitor bank (C), power supply (V), spark gap (also called thyratron switch), inductor (L), and resistors (R). Basically, a pulsed magnetic field circuit is an RLC (Resistor−Inductor−Capacitor) circuit. A simple schematic diagram for the pulsed magnetic field is shown in Figure 10.
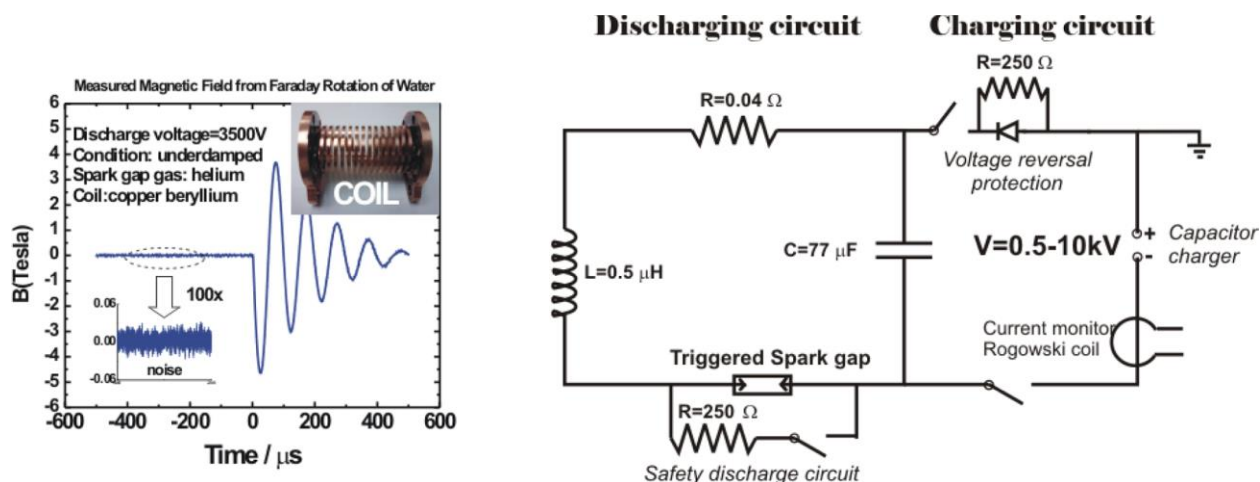
Figure 10 (Left) Experimentally determined pulse magnetic field from Faraday rotation of water. The inset shows the picture of the helical beryllium copper coil used in the experiments. (Right) Schematic circuit diagram of the pulsed magnetic field apparatus. Reprinted with permission from ref.[39] Copyright (2014) American Chemical Society

The capacitor bank is charged with a power supply. When the charged capacitor bank is discharged through the inductive coils for a short time, electric energy is transformed into magnetic energy.[45] The production of a suitably shaped magnetic field requires a current to pass through a coil, but choosing the parameters of the coil is nontrivial because of the trade-off between the magnetic field strength, the field homogeneity, and the inductance of the coil. Increasing the number of turns of the coil increases the field strength for a given current, and increasing the diameter of the coil provides a larger region of the field uniformity but decreases the field strength. An increase in either the coil diameter or number of turns causes an increase in the inductance of the coil, and so for maximizing the rate of field switching, the number of turns and coil diameter should be minimized.[46] A series of resistors controls the charging current. The value of $\pi(LC)^{1/2}$ gives the duration of the pulse.[47] The pulsed magnet constructed for this work consists of a capacitor bank of 77.3 μF of Maxwell Laboratories which is charged by a power supply/charger of Lumina Power, Inc. The power supply uses 100−240 V AC-50/60 Hz input

and output of 10 kV@500 J/s in continuous operation. All the experimental operations are controlled by the computer programmable controller. The overall discharge energy can be calculated using the expression $1/2CV^2$. Principally, the discharge of the capacitor bank tends to be critically damped which implies $R = 2 \times (L/C)^{1/2}$. The spark gap is the major resistance in the circuit, and most of the energy is dissipated through the spark gap during discharge and the remaining, negligible, energy is used in the Joule heating of the circuit.[47] A small spark gap gives the necessary resistance for the critical damping. Theoretically, the capacitor bank needs to be charged to cross the breakdown voltage of the spark gap. The breakdown voltage is the minimum voltage that causes a portion of insulator to become electrically conductive and complete the electric circuit. In these experiments the spark gap is fixed to approximately 2 mm and is triggered by using a high voltage trigger pulse generator.

The strength of the magnetic field applicator is measured via the Faraday rotation of an optical material with known optical constant.[47] The strong magnetic field induces birefringence of an optical material. Rotation of the plane of polarization of a linearly polarized light is proportional to the amount of magnetic field according to $\theta = \upsilon Bl$ where υ is Verdet constant of the material, B is the magnetic field, and l is the optical path length. The magnitude of Faraday rotation of optical materials is linearly proportional to the amount of magnetic field, which is utilized in calibrating the pulsed magnetic field for the experiments described in this thesis. For the calibration of magnetic fields, either borosilicate glass or water is used with a known optical path length. The Faraday rotation constant (Verdet constant) of these materials are published in the literature. A linearly polarized 632 nm HeNe laser is passed through the water or borosilicate glass sample. The exiting laser beam passes through an analyzer (calcite prism) oriented 45° relative to the orientation of the linear polarized light, which allows splitting the laser into two

equal intensity beams that are projected on a balanced photodiode (model 2307 large-area adjustable-gain balanced photoreceivers from Newport Inc.). The photoreceiver is placed far from the magnetic field to minimize any electronic interference from magnetic fields directly influencing the signal on the photoreceivers. When the magnetic field is present, the rotation of magnetic field appears as a positive or negative signal (depending on the direction of the magnetic field) on the oscilloscope from the balanced photodiode. On the basis of the characteristics of the photoreciever, the optical power difference and the magnitude and direction of the Faraday rotation signal are calculated. Comparing the measured signal with the value from the faraday equation of the material, the magnetic field is calculated. For the drug release studies, the peak strength of the magnetic pulse remained at approximately 3 T. The actual magnetic field profile from faraday measurement is shown in the inset of Figure 10.

2.6 Construction of Helmholtz and anti-helmholtz pulsed electromagnets for ultrasound measurements

Two identical electromagnetic coils (Helmholtz and anti-Helmholtz configuration) are constructed with opposite windings to produce homogeneous and inhomogeneous magnetic fields for ultrasonic experiments. These magnetic fields are used to help assess the ultrasound generated from single domain superparamagnetic nanoparticles. The first coil, also called the anti-Helmholtz coil, is shown in Figure 11-A,B. Figure 11-A shows the schematics of the coil winding of the anti-Helmholtz coil, and Figure 11-B shows the picture of the coil. The coil is constructed from alternatingly stacking copper and mica disks similar to the construction of bitter magnets.
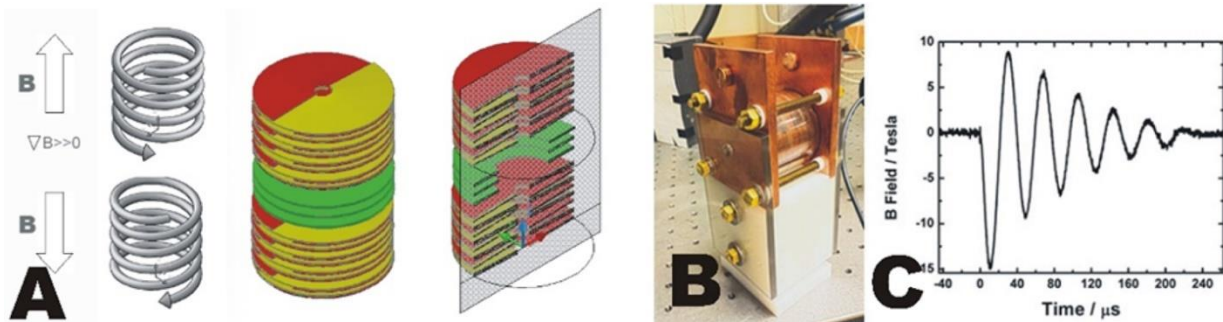
Figure 11 (A) Sketch of anti-Helmholtz coil to produce large pulsed magnetic field gradient. (B) Picture of the finished electromagnet. (C) Measured magnetic pulse by Faraday rotation of Pyrex glass. Adapted with permission from ref.[39] Copyright (2014) American Chemical Society

The anti-Helmholtz coil is optimized to produce a large magnetic field gradient, needed for the translational motion of the nanoparticles in the colloidal dispersion. The estimated maximum linear magnetic field gradient is approximately 800 T/m. In addition to the anti-Helmholtz coil, a Helmholtz coil is also prepared with parallel winding that produces homogeneous magnetic fields. The magnetic field in the Helmholtz coil is measured via the Faraday rotation of a small BK7 glass cylinder placed at the center of the Helmholtz coil. Figure 11-C shows the measured magnetic fields of the Helmholtz coil from the Faraday rotation of the BK7 glass cylinder. Both of the coils described above are integrated with electronics that are capable of producing several thousands of ampere current pulse to drive these electromagnetic coils. In the experiments, the initial coil current is kept constant throughout the experiments. The electronics are based on trigger discharged using a spark gap, which limits the lowest magnetic fields in the pulsed magnet field generator to several tesla. For coupling and measuring the generated ultrasound, one end of a 1 m long glass capillary tube filled with the colloidal dispersion of magnetic nanoparticles in water is inserted into the coil and the other end of the

capillary is mounted against an ultrasonic sensor (Benthowave, BII 7011 hydrophone). The sensitivity of the hydrophone is -198 dB µV/Pa (194.6) with a cutoff frequency of 60 kHz. The magnetic fluid used in these experiments is composed of Ferrotech EMG 607 iron oxide nanoparticles dissolved in water with the help of proprietary cationic surfactant. The size of the particles is 10 nm in diameter with an average magnetic moment of 110 G (saturation magnetization 0.011 T), viscosity <5 mPa x s, and a density of 1.1×10^3 kg/m^3 at room temperature. These particles are stabilized with ionic surfactant that ensured that the particle did not aggregate during the experiments. The concentration of the ferrofluid is 2 vol %, which has been further diluted for the experiments yielding a volume percent stock solution. The stock solution is further diluted for the concentration-dependent studies presented in this thesis.

2.7 Small amplitude AC magnetic field coils for ultrasound measurements

Small amplitude AC magnetic field coil setup consists of a setup of two coil pairs (Helmholtz or anti-Helmholtz configuration) wired with braided and insulated wire for better high-frequency response. Between the layers of windings of the coil, a layer of parafilm is used to dampen the noise from the movement of the wires. A sketch of the experimental setup is shown in Figure 12.
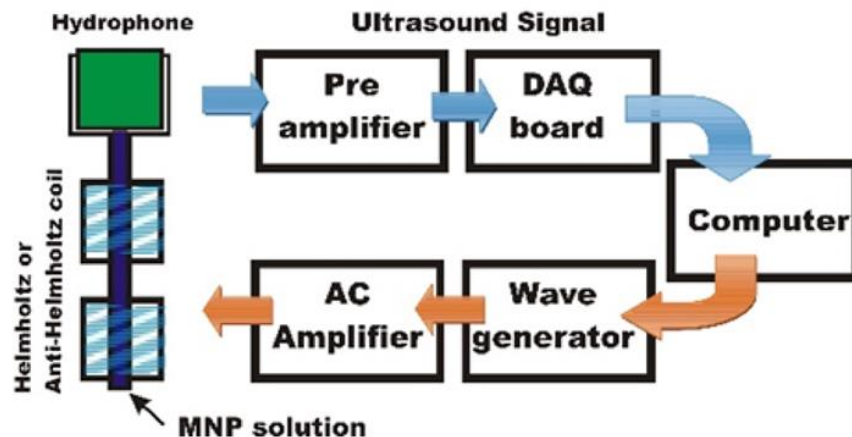
Figure 12 Sketch of the experimental setup used to detect frequency dependent ultrasounds from AC magnetic field in homogeneous and inhomogeneous magnetic fields. Adapted with permission from ref.[48] Copyright (2016) American Chemical Society.

A frequency generator is used to generate continuous sinusoidal wave that is further amplified to produce sinusoidal magnetic fields at variable frequency in the coil pairs. Between the coil pair, a glass tube is inserted filled with the MNP dispersion. At the end of the glass tube a broad frequency response (10−500kHz) hydrophone (BII-7043 Directional Broadband Hydrophone) is inserted. The signal from the hydrophone is amplified with a low impedance voltage preamplifier and digitized with a 2M sample/s 16 bit DAQ board. The time-domain signal is Fourier filtered so that only the signal at the drive frequency is detected and recorded on the computer. For each measurement, the background signal of water was also collected and subtracted from the data presented in this thesis. The solution of proprietary surfactant is also tested for ultrasound generation, and it has showed the same amount of ultrasound as the water produced. In order to ensure uniform power transfer by the broadband amplifier, the frequency-dependent current has been measured with a current sensor (Rogowski coil). To remove the frequency-dependent response of the hydrophone, the data are normalized to the frequency response of the hydrophone from the 10 to 500 kHz frequency range.

Chapter 3 - Nested Helmholtz coil design for producing homogeneous transient rotating magnetic fields

3.1 Introduction

Rapidly changing magnetic fields are utilized in many areas of science and engineering. In the field of life science, one important area where magnetic fields are utilized is the field of magnetic hyperthermia,[49] where the alternating or rotating magnetic fields are utilized to produce heat in the sample via Neel or Brownian relaxation of magnetic nanoparticles.[50] Generally, magnetic nanoparticles can produce useful heat on the order of a few 100 W/g.[49, 51] Recently, Lee et al.,[52] have shown that if the exchange interaction of the magnetic nanoparticles is used, the number can reach 1000 W/g quantities. Recently, Sharapova et al., have shown that by using rotating magnetic fields instead of alternating magnetic fields, the heating efficiency of magnetic nanoparticles has increased significantly.[53] In traditional magnetic hyperthermia, the magnetic field used is a low amplitude sinusoidal magnetic field.[49] In general, the produced heat is capable of destroying cancer tissue or releasing drug molecules from liposomes[39] for targeted delivery. However, there are several challenges of this technology so that it reaches its full potential. The required nanoparticle concentration for effective elimination of cancer tissue needs to be on the order of several mg/ml to reach needed 42-45 ℃ temperature.[38, 54] In addition, magnetic hyperthermia treatments last for several minutes and hours. A more effective way to destroy cancer cells is to utilize the nanoparticles as little magnetically driven drill bits. The mechanical force[55] can potentially be more effective in eliminating cancer cells if the lipid bilayer can be punctured.[56] Recent results have shown[57] that cancer cells are more deformable than healthy

cells, which could be utilized in selective cancer cell destruction if combined with mechanical force from rotating or twisting magnetic nanostructures as a result of external magnetic stimuli. In order to rotate magnetic nanoparticles on the order of 10 to few tens of nanometer size scale, the magnetic field needs to be increased to overcome the thermal motion of the particles. The required rotating magnetic field strength to manipulate magnetic nanoparticles on the 10-30 nm diameter range is on the order of a few hundred millitesla. A simple way to generate rotating magnetic fields is via a pair of Helmholtz coils arranged perpendicularly. These designs are widespread and can produce magnetic fields that are few millitesla. Increasing the magnetic field beyond this point is challenging because the continuous current can result resistive heating which requires significant amount of cooling. Cooling of the coils can be facilitated at larger facilities such as the National High Magnetic Field facility. However, the laboratory use of these strong rotating magnets without cooling is desirable for life science based research. In this chapter, a low duty cycle nested Helmholtz coil system is described. It is capable of producing strong rotating magnetic pulses without the need of significant cooling.

3.2 Construction of nested Helmholtz coils

Traditionally, Helmholtz coils are used to generate uniform homogeneous static and alternating magnetic fields in a relatively large volume. The Helmholtz coil design is also used to produce homogeneous rotating magnetic fields when two or three coils are nested within each other. Manipulating the currents inside these coils allows the production of static and rotating magnetic fields in the three-dimensional space. Unfortunately, the traditional wire coiling used in Helmholtz coils has its limitation in increasing the strength of the magnetic fields. There are

several design challenges of producing strong rotating magnetic fields in a relatively large volume. Early on, Bitter[58] developed a design based on stacking of concentric discs that minimizes the forces acting on the coil. The current density in traditional solenoid type coils is constant, while in the Bitter coil designs, the current density falls with 1/r producing a more favorable condition for high magnetic fields. The additional advantage of the bitter coil design is that it distributes the mechanical stress from the Lorentzian force more evenly than in the wire coiled solenoid and also allows efficient cooling if holes for liquid coolant are introduced in the bitter disks.
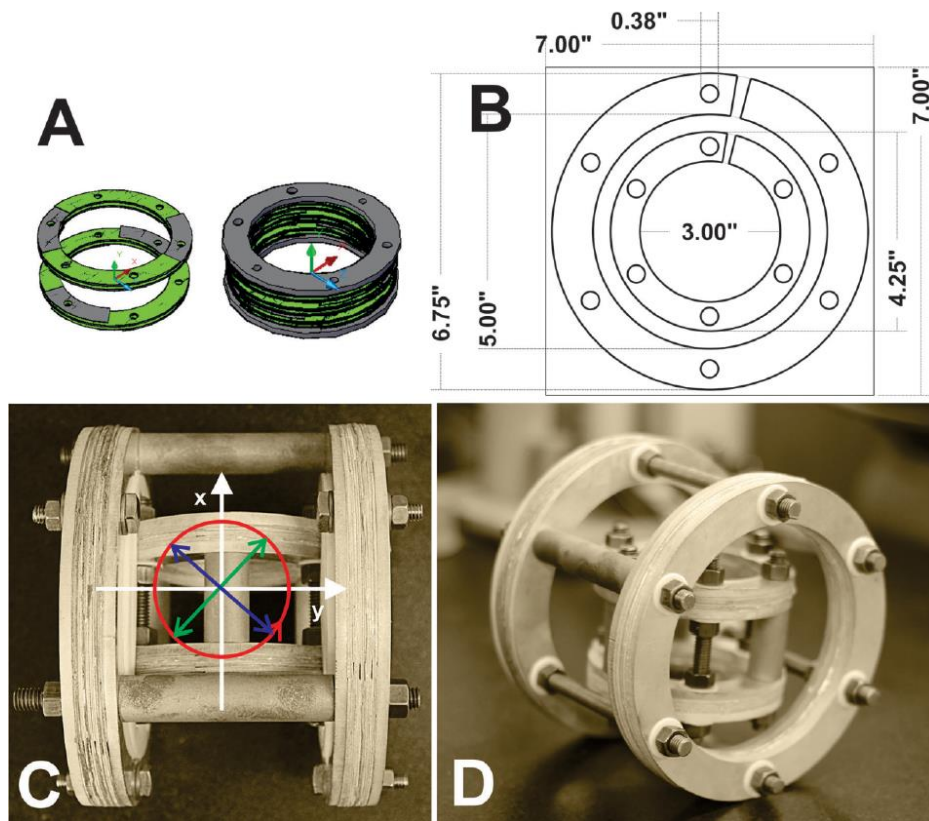
Figure 13 (a) Assembly of the bitter disks. (b) Dimensions of the bitter disk used to produce the nested Helmholtz coil. (c) Top view of the Helmholtz coil indicating the directions of the magnetic field produced in this paper. (d) Perspective picture of the nested Helmholtz coil without the Teflon insert. Reprinted from ref. [59] with the permission of AIP Publishing.

In this thesis, a merged of the Bitter design of electromagnet (Figure 13) is used, to form a 2D Helmholtz coil system for producing rotating magnetic fields. The Bitter disks are manufactured from copper-beryllium alloy to increase the tensile strength of the coil material to resist the mechanical stress from the Lorentzian forces. The tensile strength of copper is 220 MPa while the copper-beryllium used in this work has a tensile strength of 820 MPa. The conductivity of copper-beryllium (1/2 HT tempered C17410 alloy) is 50% of the conductivity of copper. The Bitter disks are electrochemically plated with silver, which further increases the conductivity of the coils and reduces the contact resistance. The bitter disks are separated by mica sheets and sandwiched between the silver coated copper end plates. The packing order and the assembly of the bitter disks are also shown in Figure 13. The two parts of a single Helmholtz coil are held together by brass rods that are insulated from the electrical components of the coils. The spacers between the two parts of the coil are manufactured from high conductivity copper rods. These rods are also silver plated for optimal conductivity. The smaller nested Helmholtz coil is assembled with the help of a Teflon insert, which secures the smaller coil inside the larger coil. The Teflon insert can be rotated with the inner coil so that the main rotating axis of the rotating magnet can be changed.

3.3 Results and discussion

The nested Helmholtz coils are calibrated with the help of 60 Hz alternating current from the electrical outlet. 12A RMS current is passed through both of the coils, and the magnetic fields of the two coils are measured with a low frequency AC Gauss meter. The output from the Gauss meter has been recorded and shown in Figure 14.
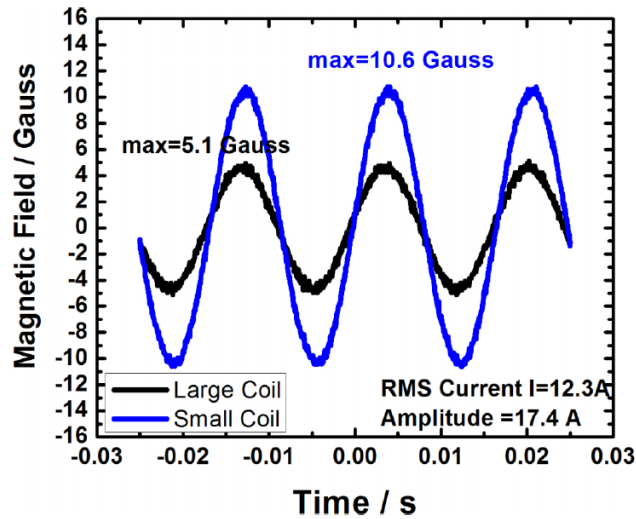
Figure 14 The graph shows the measurement of the magnetic field of the nested Helmholtz coils from low frequency alternating current from the electrical outlet. Reprinted from ref. [59] with the permission of AIP Publishing.

The results from Figure 14, show that in order to achieve the same magnitude magnetic fields at the center of the two coils for the circular polarized fields, approximately twice as much current has to pass through in the larger coil than in the smaller coil. In these experiments, the current in the larger coil is increased by using higher discharge voltage in that coil. By careful choice of the number of disks used in each coil, the same amount of magnetic fields can be achieved with the same amount of current. The data in Figure 14 also allows calibrating the Rogowski coils used in the high voltage experiments. The rotating magnetic field is produced by discharging high voltage capacitors via the coils of the Helmholtz magnet. The circuit design is shown below, in Figure 15 for a single Helmholtz coil. Two identical circuits are used to control the magnetic field independently from each of the nested Helmholtz coils. One of them is shown in Figure 15. The capacitor is discharged with the help of a homemade triggered spark gap as shown in Figure 15. The trigger pulse is a high frequency 0.5 J 20 kV pulse with a duration of

500 ns that initiates the trigger after charging the main capacitor. The high frequency current is monitored by a homemade Rogowksi coil, which produces voltages proportional to the dI/dt in each coil. The voltages are measured by attenuated probes and recorded by an oscilloscope.
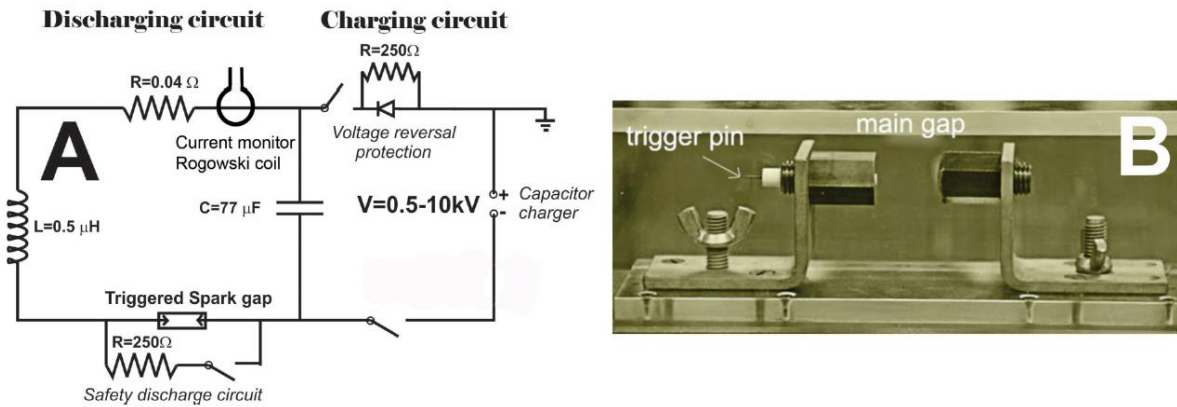
Figure 15 (a) Schematics of charging and discharging circuit of a single coil for nested Helmholtz coil design. (b) Picture of the homemade spark gap with adjustable gap. Reprinted from ref. [59] with the permission of AIP Publishing.

The signal is then integrated to produce the current response of the coils. The two independent discharge circuits for each of the Helmholtz coils are connected via a digital transistor-transistor logic (TTL) timing box, which allows precise control of the magnetic pulses with respect to each other. The TTL pulses are used for timing signal to trigger the spark gaps of each coil independently.

The magnitude of the magnetic field applicator is also measured via the Faraday rotation of an optical material, such as water or borosilicate glass, with known optical constant (Figure 16).[47] This procedure is necessary to ensure that the electrical sensor properly functions at both low and high magnetic fields. The optical measurement of the magnetic field of the coils is as

follows: The strong magnetic field induces birefringence of an optical material. The induced

birefringence of the material rotates the plane of polarization of a linearly polarized light.
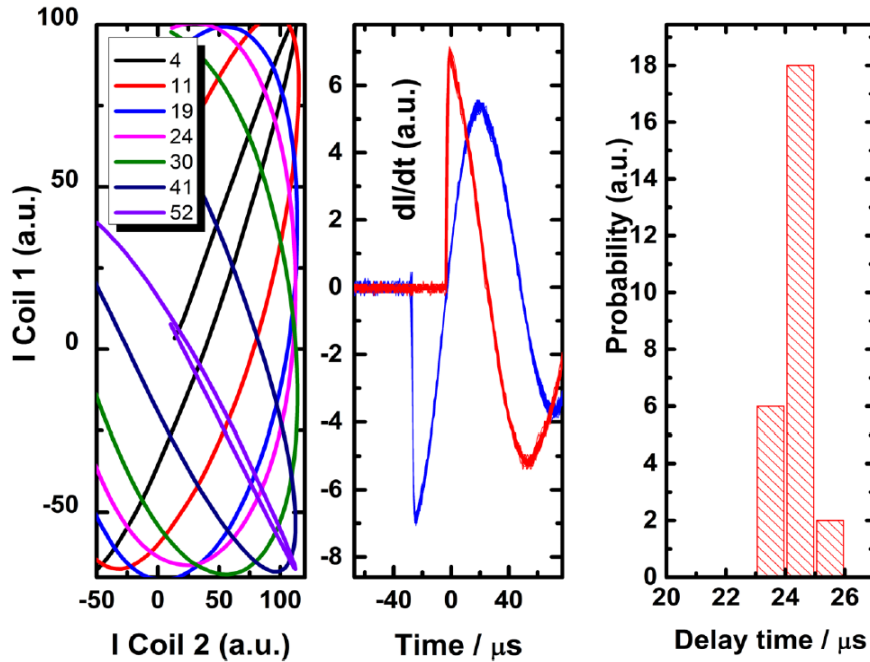
Figure 16 LEFT: (a) Current signal from the two coils of the nested Helmholtz coils with various time delays. MIDDLE: (b) Direct signals from the Rogowski coils for the inner and outside Helmholtz coil from 26 simultaneous discharges. RIGHT: (c) Histogram of the timing jitter of the inner and outside coil firing from 26 shots. Reprinted from ref. [59] with the permission of AIP Publishing.

The rotation angle (Θ) varies according to Faraday equation: $\Theta = \nu B l$, where ν is Verdet

constant of the material, B is the magnetic field, and l is the optical path length. The magnitude

of the Faraday rotation of optical materials is linearly proportional to the amount of magnetic

field, which is utilized in the calibration of pulsed magnetic fields for the experiments described

in this chapter. For the calibration of magnetic fields, water is used with known optical

pathlength (1 cm). The Faraday rotation constant (Verdet constant) of these materials is

published in the literature.[60] A linearly polarized 632 nm HeNe laser is passed through the water

or borosilicate glass sample. The exiting laser beam passes through an analyzer (calcite prism) oriented 45º relative to the orientation of the linear polarized light, which allows splitting the laser into two equal intensity beams that are projected on a balanced photodiode (Model 2307 Large-Area Adjustable-Gain Balanced Photoreceivers from Newport, Inc.). The photoreceiver is placed far from the magnetic field to minimize any electronic interference from magnetic fields directly influencing signal on the photoreceivers. When the magnetic field is present, the rotation of magnetic field appears as positive or negative signal (depending on the direction of the magnetic field) on the oscilloscope from the balanced photodiodes. Based on the characteristics of the photoreciever and the optical power difference, the magnitude of the Faraday rotation signal is calculated.
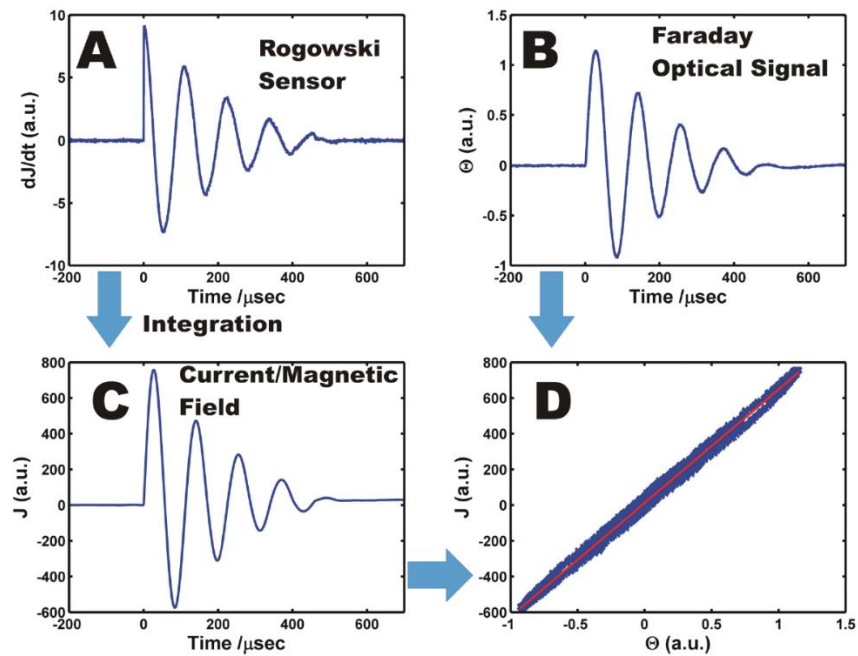
Figure 17 (a) signal of the current through Rogowski sensor (b) optical measurement of the Faraday rotation of water placed inside the coils (c) current/magnetic field (d) magnitude and direction of magnetic fields inside the coils for the rotating magnetic fields. Reprinted from ref. [59] with the permission of AIP Publishing.

By comparing the measured signal with the value from the Faraday equation of the material, the magnetic field is calculated. In Figure 17, the magnetic field of coil is measured via electronic sensor from the Rogowski coil (a) and the measurement of the Faraday rotation (b) of water placed inside the coils. For this calibration procedure, only one of the coils is fired. The direction of magnetic field is parallel to the 632 nm laser used for the Faraday measurement. The integrated Rogowski signal (c) is linearly proportional to the signal from the optical measurement (d). After calibration, the signals from the two Rogoswki sensors allow monitoring the magnitude and direction magnetic fields inside the coils for the rotating magnetic fields.

Figure 17 demonstrates that the signal from the Rogowski sensor and the optical measurement are linearly proportional. Therefore, both measurements can be used to evaluate/calculate the magnetic fields of the coils. In the experiments below, the signals from the Rogowski coils are used as an indicator of the magnetic field strength. Figure 16(a) shows the effect of changing the delay between the magnetic pulses on the two different coils, which results in different shaped magnetic fields. Changing the timing, the coils can produce linear alternating magnetic fields or rotating magnetic fields. Figure 17(b) shows the direct output from the Rogowski coil pairs fixed at a given time delay. This signal is integrated to obtain the current signal as described earlier. The direction of the rotating field can be also manipulated by changing the initial direction of the current in the coils resulting in left or right rotating magnetic fields. The maximum discharge of the capacitors used in the experiment is 10 000 V, which corresponds to 2850 J of energy. In a single shot, the maximum calculated temperature increase of the coil from this energy is 1.6 ºC based on the weight of the copper coils and its heat capacity, but in reality, it is probably much less than that since this simple estimate does not take the weight of the cables and the capacitor into account.

The measured rotating magnetic field amplitude is 200 mT at full discharge (10 000 V charge for the larger coil). This is about 2.5 times less magnetic field than what is calculated from modeling the discharge circuit and comparing the current with the data from Figure 14. With careful optimization of the contact points in the coils, the current can possibly be further increased, resulting in better agreement between the theory and practice. Timing of the magnetic pulses is important so that the desired rotating fields can be produced. The data on the time reproducibility (Figure 16), of the magnetic pulses indicate that the jitter of the triggering in this system is relatively low. The timing jitter of the relative trigger remains under 1 μs,[61] which allows accurate timing to produce rotating fields for the few tens of kilohertz underdamped magnetic pulses.

Finally, it is important to match the inductance of the coils to produce pulses where the current and magnetic pulses remain in phase for the entire duration of the rotating magnetic field. This is demonstrated in Figure 18, which shows two separate cases. When the inductances of the coils are not matched, the various time delays will result in "scrambled" magnetic pulses.
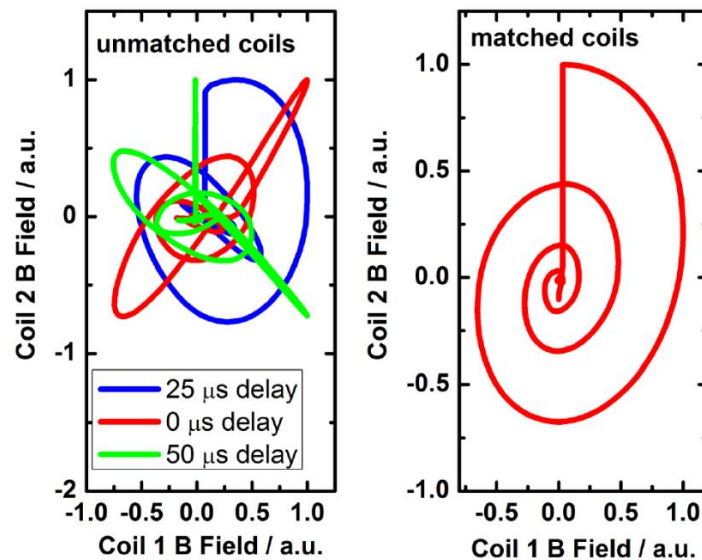
Figure 18 LEFT unmatched Helmholtz coil RIGHT matched Helmholtz coil. Reprinted from ref. [59] with the permission of AIP Publishing.

When the inductances of both coils are matched with the help of installing additional cable length to one of the coil circuits, the magnetic pulses become identical in both coils, which yield the desired rotating magnetic pulses. The magnitude of the rotating magnetic field is calculated from the current measurements from the Rogowski coils during the high voltage discharge. In order to test the homogeneity of the rotating magnetic field, calculation is performed by using finite element method (FEM) implemented with COMSOL Multiphysics (Burlington,MA). This 3D model includes two pairs of coils, with the larger coil centered on the y-axis, and the smaller coil centered on the x-axis. The model specifies a current density on each coil (out of phase) and solves for the magnetic vector potential and field strength at 100 kHz.

Figure 19 illustrates the homogeneity of the calculated rotating magnetic field amplitude (log(H)) for a 100 kHz continuous operation of the in different planes for the nested Helmholtz used in the experiment. The calculation shows that the rotating magnetic field is uniform in all directions in the center of the nested Helmholtz coils.
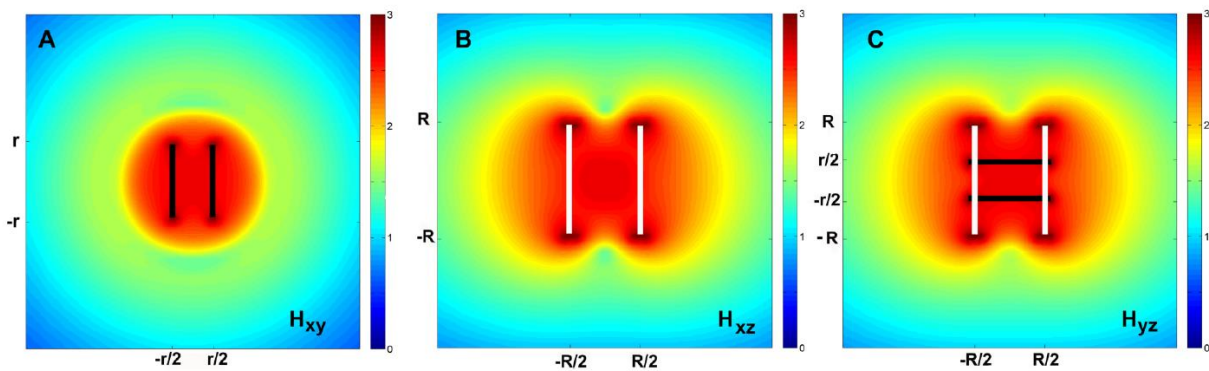
Figure 19 Calculated rotating magnetic field amplitude (log(H)) for a 100 kHz continuous operation of the in different planes for the nested Helmholtz used in the experiment. r is the radius of the smaller inner coil and R is the radius of the larger outer coil. Reprinted from ref. [59] with the permission of AIP Publishing.

The modeled region is discretized with an inhomogeneous tetrahedral mesh, including 81398 elements. A frequency domain iterative solver (geometric multigrid) is used to compute the magnetic field strength at all points in the simulation domain. The variation of the magnetic field amplitude inside the inner coil is few percent relative to the absolute magnitude of the magnetic field. The calculation presented above is shown for the idealized 2D Helmholtz coil.

The dimension of experimental coils used here shows a few percent deviation from the idealized Helmholtz coil; with careful adjustment of the manufacturing process, the coil can very closely approximate the idealized 2D Helmholtz coil.

3.4 Conclusions

The construction and operation of a novel Helmholtz are demonstrated to generate strong rotating magnetic field. The design shows scalability by manipulating several factors: increasing the number of plates used to construct the coils, reducing its dimensions, and increasing discharge voltage. The nested Helmholtz coil design could also be used in magnetic hypothermia experiments where minimizing the resistive heating is important at high frequencies due to the skin effects of the current at several tens of kilohertz.

Chapter 4 - Pulsed Magnetic Field Induced Fast Drug Release from Magneto Liposomes via Ultrasound Generation

4.1 Introduction

Liposomes were first described in 1961 (published 1964[62]) by Alec Bangham. Liposomes (and the payload that they have trapped inside during formation), can be separated from smaller molecules simply by gel filtration or dialysis, making them very useful delivery agents.[63] Liposomes are stable in blood, not releasing their contents,[64] and when incubated with plasma constituents, they retain their spherical shape.[65] Liposomes made from L,α-dipalmitoylphosphatidylcholine (DPPC) are widely used for the intravenous delivery of drugs, because they are not prohibitively expensive and feature suitable biophysical properties. The higher phase transition temperature (Tm) of DPPC is 314 K. At T > Tm liposomes can be filtered through porous membrane filters, which make spherical unilamellar liposomes with a very small polydispersity available.[66] The fast removal of the liposomes by the macrophages and monocytes of the reticuloendothelial system can be prevented by attaching a polyethylene glycol coating to the outside of the liposome.[67] Polyethylene glycol apparently creates a steric block around the outside of the liposome that does not interact with recognition molecules. Since the polyethylene glycol does not interact with recognition molecules and it prevents the recognition molecules from reaching the liposomal surface, the liposomes are widely ignored by the reticuloendothelial system. The liposomes prepared this way (liposomes coated in polyethylene glycol) have come to be known as stealth liposomes.[67] To date, several liposomal drug delivery systems have been

developed (e.g., Nicoderm and others)[37] that rely on the slow release of their payload. However, for the treatment of cancer or infectious diseases, it is certainly desirable to deliver the payload (drug) at once after the target has been reached. As stated in chapter 1, AC-magnetic hyperthermia was used to trigger the release of magneto liposomes' payload by heating magnetic nanoparticles until the liposomes either burst or dissolve in the surrounding aqueous medium.[38] The main disadvantage of AC-magnetic hyperthermia is that the payload can be damaged by heat and the release is not fast. In this chapter, a method is presented for the immediate release of the liposomes' payload without a significant increase in (local) temperature (less than 2-3 $^{\circ}$C). This goal is achieved by using the mechanical motion of the magnetic nanoparticles that are embedded within either the cores of the lipid bilayers of the liposomes, or at the interface between core and bilayer.

The liposomes used here feature comparatively low diffusion coefficients. Without an external stimulus, they will retain their payload for extended periods of time.[68] To meet this challenge, the cholesterol content of their lipid bilayers is adjusted. The mechanical motion of the magnetic nanoparticles locally destabilizes the lipid bilayer and causes its collapse and the subsequent release of the liposomes' payload. In contrast to the heat-induced release of drug from magneto liposomes from AC magnetic fields, the drug release takes place due to mechanical motion of magnetic nanoparticles, therefore producing a significantly smaller amount of residual heating. The successful application of the mechanical force on the nanoparticles to create controlled disruption in a lipid bilayer places some limits on the nanoparticles and magnetic fields that can be used in the experiments.

4.2 Results and discussions

4.2.1 Liposome Release Studies with MgSO$_4$

The triggered drug release of the magneto liposomes is tested via the release of conductive MgSO$_4$ from the liposomes upon exposure to pulsed magnetic fields. In Figure 20, a Bode plot is presented, containing the data from liposomes and HEPES (4-(2-hydroxyethyl)-1-piperazine ethanesulfonic acid) buffer are in solution.
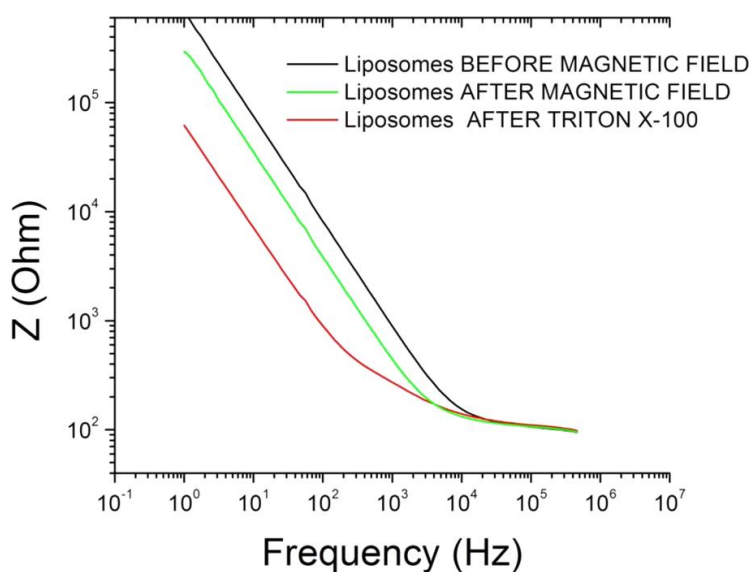
Figure 20 Bode plot of a magneto liposome solution before and after the application of magnetic fields. Addition of TRITON X-100 destroys the liposomes and releases all the MgSO$_4$. Reprinted with permission from ref.[39] Copyright (2014) American Chemical Society.

The black line in Figure 20 represents the liposomes, which contain superparamagnetic nanoparticles and MgSO4, mixed with HEPES Buffer. Then the magneto liposomes were

exposed to the strong pulsed magnetic field pulses 10 times. The green line represents the

magneto liposomes and HEPES buffer after exposure to the magnetic field. As expected, there is

a decrease in impedance (increase in conductivity) because at least some of the liposomes

released their payload of $MgSO_4$. The red line is the magneto liposomes after exposure to Triton

X-100. Triton completely destroys all of the liposomes; however, it also contributes to the

conductivity. To remove any side effects from the contribution of Triton X-100 to the overall

conductivity, the magneto liposomes are also destroyed with a sonic dismembrator. After the

sonication, the sample is left to equilibrate with room temperature for 10 min to remove the

temperature-dependent bias of the conductivity measurement. The results are summarized in

Table 1, which shows the $MgSO_4$ release from magneto liposome after application of 10

magnetic pulses.

	Before magnetic pulse	After magnetic pulse	After sonication	Percent release	Average
Liposome 1	5676	4740	3635	48.5%	47.7±1.9%
Liposome 2	4786	4325	3782	49.2%	
Liposome 3	5459	4734	3802	45.6%	
Control 1	4129	4177	3496	-1.2%	-9.5±8.3%
Control 2	3521	3523	3243	-9.5%	
Control 3	3971	3709	3338	-17.8%	

Table 4-1 Summary of AC Impedance Measurements of Magneto Liposomes Exposed to 10 Magnetic Pulses. Reprinted with permission from ref.[39] Copyright (2014) American Chemical Society.

The individual values show the resistance of the solution at 214 Hz and the concentration of the $MgSO_4$ is calculated from a formula obtained by fitting the $MgSO_4$ calibration curve (Figure 7) ($CMgSO_4 = ((\sigma-0.00031)/0.000844)^2$). Here σ is the conductivity of the sample at 214 Hz expressed in 1/ohm. The control liposomes do not contain magnetic nanoparticles.

In addition to the data presented in the Table 4-1, experiments are also conducted to assess how many pulses are needed to release the $MgSO_4$ from the magneto liposomes. Figure 21 shows the impedance measurement of magneto liposome solution following exposure to single magnetic pulses.
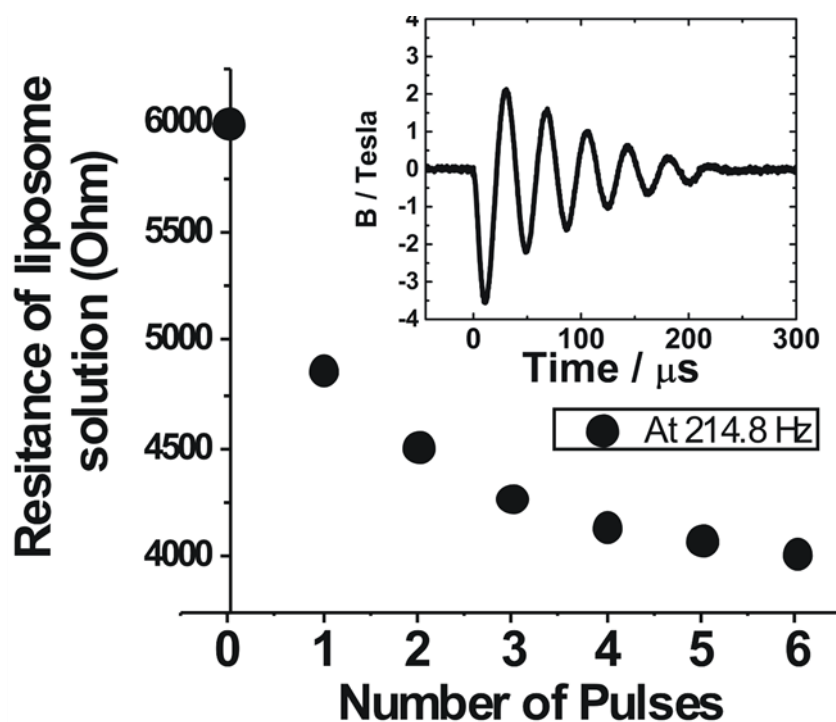
Figure 21 Impedance changes of the magneto liposome solution upon exposure to subsequent magnetic pulses. Reprinted with permission from ref.[39] Copyright (2014) American Chemical Society.

This measurement indicates that a single magnetic pulse releases a significant portion of the $MgSO_4$ from the liposome. The magnetic pulses did not produce any noticeable heating of the magneto liposomes.

4.2.2 Liposome Release Studies with 5(6)-Carboxyfluorescein Dye.

The typical fluorescence emission spectra are shown in Figure 22. Same measurements are performed as for other NPs. The clear difference can be seen in the fluorescence emission spectra between the control liposome and magnetic NPs loaded liposome.
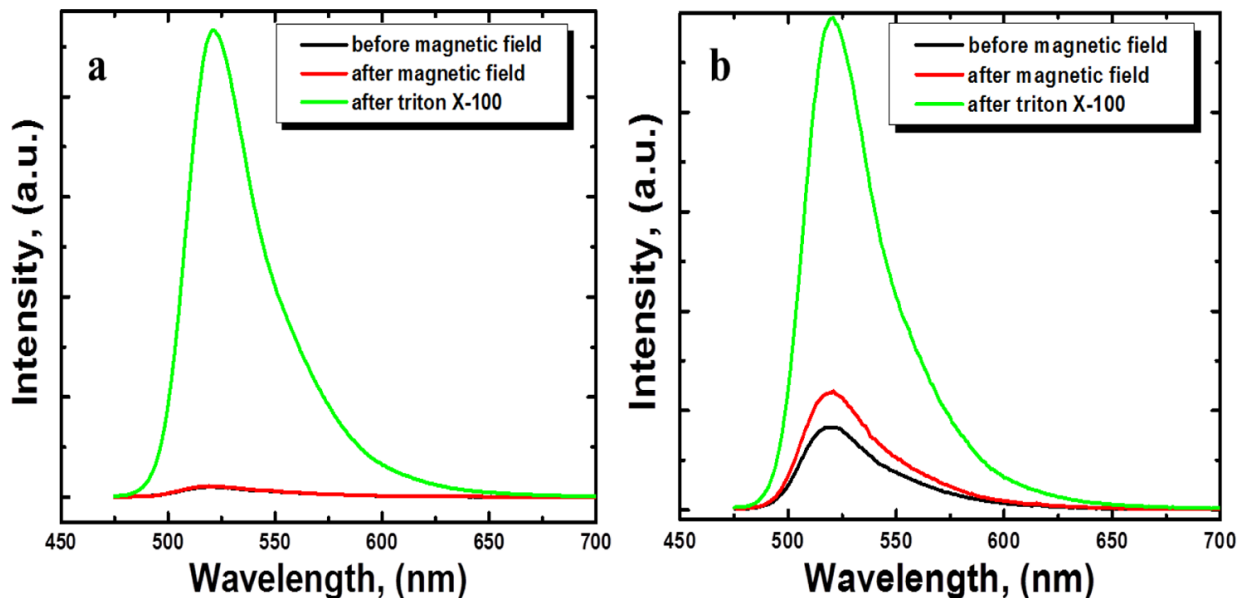
Figure 22 Static fluorescence emission measurements of (a) control liposome, no NP; (b) magnetic NPs (Fe$_3$O$_4$)-loaded liposome, before/after exposure to pulsed magnetic field and after the release of all dye as model drug using Triton X-100. Reprinted with permission from ref.[39] Copyright (2014) American Chemical Society.

To quantify the result, the percentage release of the drug is calculated. The percentage release of the drug is calculated from the integrated fluorescence intensity of the emission spectra. The calculated surface areas under the emission spectra are used to calculate the percentage release as:

$$\%release = \frac{SA_{AMF} - SA_{BMF}}{SA_{AT} - SA_{BMF}} \times 100$$

where SA_{AMF} is the surface area after exposure to magnetic field, SA_{BMF} is the surface area before exposure to magnetic field, SA_{AT} is the surface area after the addition of Triton X-100. The calculated % releases for control liposomes and Fe_3O_4 NPs loaded liposomes are tabulated in Table 4-2.

Samples	SA_{BMF}	SA_{AMF}	SA_{AT}	% release
Liposome	1.22×10^6	1.27×10^6	1.07×10^7	0.12
Liposome with Fe_3O_4	2.13×10^6	2.96×10^6	1.20×10^7	8.40

Table 4-2 Drug Release Data for Control and Magnetic NPs Loaded Liposomes. Reprinted with permission from ref.[39] Copyright (2014) American Chemical Society.

The same experiment is repeated as described above with the hydrophobic, hydrophilic, and amphiphilic peptide-coated Fe_3O_4 NPs, since depending on the surface property of NPs, the position of the NPs in the liposomes is fixed. The % releases of drug are calculated which are given in the following Table 4-3. The percentage releases with hydrophilic and amphiphilic peptide-coated Fe_3O_4 NPs are almost the same.

Samples	SA_{BMF}	SA_{AMF}	SA_{AT}	% release
Hydrophobic	4.61×10^6	4.77×10^6	1.07×10^7	0.24
Hydrophilic	5.50×10^6	7.28×10^6	5.00×10^7	3.57
Amphiphilic	2.77×10^6	4.52×10^6	5.09×10^7	3.63

Table 4-3 Drug Release Data for Hydrophobic, Hydrophilic and Amphiphilic Peptide Coated Fe_3O_4 NPs Reprinted with permission from ref.[39] Copyright (2014) American Chemical Society.

The percentage release with hydrophobic peptide-coated Fe_3O_4 NPs is comparatively small. This indicates that the hydrophobic peptide-coated Fe_3O_4 NPs are not incorporated in the liposomes because of the surface property of NPs. As it has been shown above, when liposomes,

filled with magnetic nanoparticles, are exposed to a short magnetic pulse, model drug molecules are released quickly from the liposomes. In a recent study, Hu et al.,[69] have demonstrated that application of magnetic pulses in the presence of magnetic nanoparticles leads to ultrasound generation. They used the resulting ultrasound for imaging purposes to reconstruct an image of an object filled with magnetic nanoparticles. Their observation is relevant to this work because ultrasound is also commonly used on liposomes to release their content.[70] To explore if ultrasound is generated from our magnetic pulses, iron oxide magnetic nanoparticles were exposed to pulsed magnetic fields. In order to assess accurately if the homogeneous or the inhomogeneous magnetic fields are more effective to generate ultrasound, two electromagnets have been developed that are very similar in construction. Detailed construction and properties of the two electromagnets build is described in Chapter 2.6. The sketch of the first magnet consists of an anti-Helmholtz coil shown in Figure 23 A and B to produce the large inhomogeneous magnetic field on the order of 400 T/m in a 3 mm center part of the coil.

In an anti-Helmholtz coil the winding of the coil pairs are in opposition to produce the large inhomogeneous magnetic fields. The second coil (Helmholtz coil) is also prepared with opposite winding that results in ~15 T homogeneous magnetic field in the full length of the coil (~50 mm). The magnetic field of the Helmholtz coil has been measured by optical method from the Faraday rotation of a small Pyrex rod (Figure 23-C). To quantify the amount of ultrasound the concentration of the nanoparticles is varied inside a glass tube that is attached to a commercially available hydrophone (BII-7011 from Benthowave Instrument Inc.) as is shown in Figure 23-D.
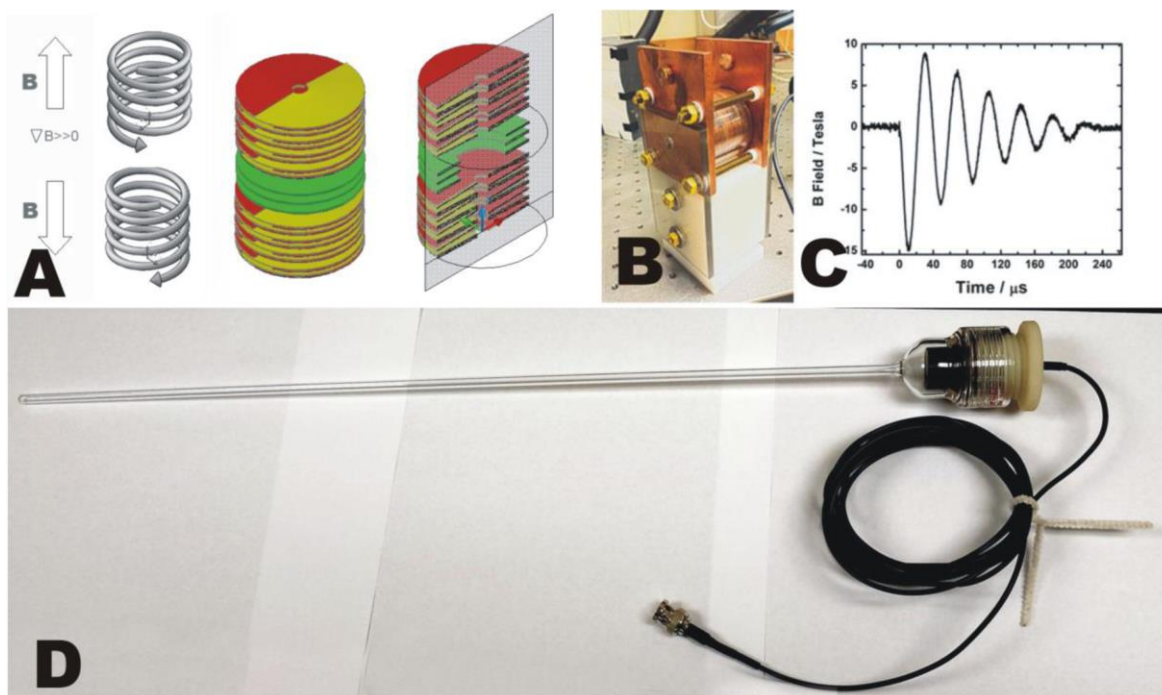
Figure 23 (A) Sketch of anti-Helmholtz coil to produce large magnetic field gradient. (B) Picture of the finished electromagnet. (C) Measured magnetic pulse by Faraday rotation of Pyrex glass. (D) Picture of the experimental apparatus used to detect ultrasound generated from pulsed magnetic fields in the presence of magnetic nanoparticles. Reprinted with permission from ref.[39] Copyright (2014) American Chemical Society.

In order to accurately assess the amount of ultrasound from the magnet, the signal from the hydrophone is recorded as a function of iron oxide concentration including the water as a reference. Figure 24 summarizes the results from the experiments to assess ultrasound generation from magnetic nanoparticles. Figure 24-A shows that current derivative as a function of time along with the hydrophone signal for water and iron oxide magnetic nanoparticle solution.

The presented results are for the Helmholtz coil, but very similar results are obtained for the anti-Helmholtz coil as well. The ultrasound power is calculated from the Fourier transform power coefficient of the actual signal. Figure 24-B shows the Fourier power coefficients for the time-dependent signal from water and from iron oxide NP solutions with increasing concentrations. The integrated power coefficients are plotted against the concentration of nanoparticles (shown in Figure 24-C).
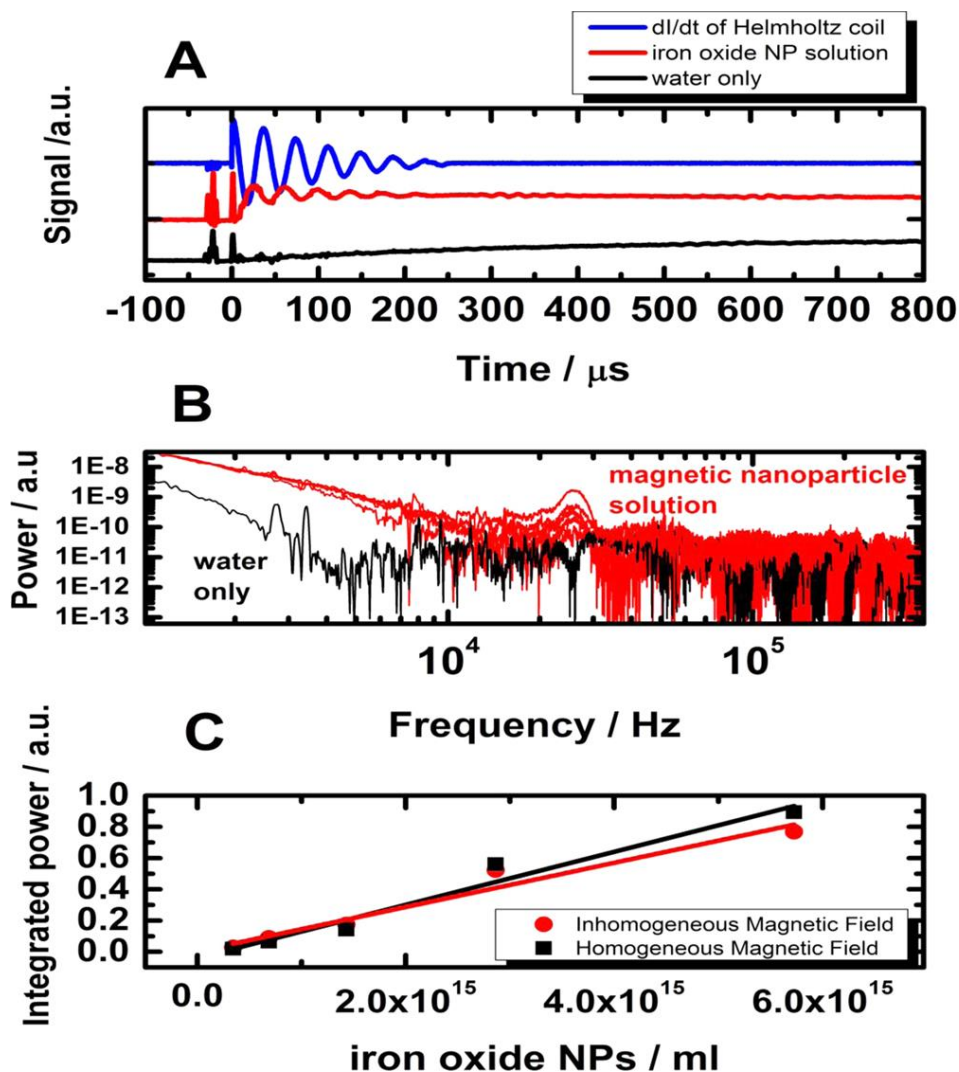
Figure 24 (A) Hydrophone signal from iron oxide NP, water in homogeneous magnetic field. As a reference the current derivative of the coil is shown. (B) Fourier power coefficient of the time-dependent signal of the NPs in homogeneous magnetic fields. (C) Concentration dependence of the ultrasound signal for the homogeneous and inhomogeneous magnetic field. The 100% concentration corresponds to the 0.31 volume% of EMG 607 iron oxide 15 nm in diameter NPs from Ferrotech Corporation. Reprinted with permission from ref.[39] Copyright (2014) American Chemical Society.

From these results, it is clear that magnetic nanoparticles generate a significant amount of ultrasound whether the magnetic field is homogeneous or inhomogeneous. Ultrasound is commonly used to disrupt the membranes of liposomes; therefore, we propose that the ultrasound generation process from the magnetic nanoparticles residing inside the liposomes is the important underlying mechanism for the disruption of lipid bilayers. The results indicate that

both magnets produce ultrasound that is significant compared to the water background at frequencies corresponding to the frequency of the pulsed magnet (~30 kHz). In the previous study by Hu,[69] the primary mechanism for ultrasound generation was the linear acceleration of magnetic nanoparticles in the inhomogeneous magnetic fields; however, here we observe that the homogeneous magnetic fields also produce a significant amount of ultrasound. It appears that at lower concentrations the inhomogeneous magnetic field has a larger contribution to the ultrasound generation. (Note that the inhomogeneous magnetic field only impacts 3 mm center part of the coil and the homogeneous magnetic field affects the entire length of the coil.) While Hu et al. proposed that only inhomogeneous magnetic fields result in noticeable amount of ultrasound, the data here indicate that homogeneous magnetic fields can also result in ultrasound. The literature indicates[71] that in strong magnetic fields the magnetic nanoparticles form chains of magnetic beads[72] and during this process the displacement of liquid results in ultrasound generation. When the magneto liposomes are exposed to magnetic fields, due to the relatively large concentration of magnetic nanoparticles inside the liposome, the generated ultrasound can significantly contribute to the drug release observed under these experimental conditions.

4.3 Conclusions

Here the fast release of model drug molecules ($MgSO_4$ and 5(6)-carboxyfluorescein) from magneto liposomes loaded with Fe_3O_4 NPs or FePt nanoparticles is demonstrated with the help of strong magnetic pulse(s). The experiments indicate that ultrasound is generated from magnetic nanoparticles in the presence of pulsed magnetic fields, which is proposed to play a key role in the release of the drug molecules from magneto liposomes. The process can be further optimized to maximize the amount of drug release based on the solubility of MNPs and the ligand coating of the nanoparticles, but no major difficulty is anticipated.

Potential Applications: (1) Instantaneous delivery of drugs with both temporal and spatial precision. (2) Delivery of therapeutic agents for cancer therapy. (3) Delivery of painkiller drug

locally following the injection of the drug loaded into magneto liposomes via intravenous therapy. (4) Experimental tool to induce instant repeated physiological changes from drugs, therefore allowing kinetic studies in living systems. (5) Release of radiation-preventive drugs from magneto liposomes induced by the strong electromagnetic field from a nuclear explosion. (6) Manipulating/modulating cellular permeability via mechanical force from the pulsed magnetic fields.

Chapter 5 - Magnetic Field Induced Ultrasound from Colloidal Superparamagnetic Nanoparticles

5.1 Introduction

In a recent study, Kinsohita et al.[73] have shown that the blood-brain barrier can be made penetrable for drug molecules via application of focused ultrasound. A crucial barrier for more effective use of the blood-brain barrier opening is the relatively low penetration of ultrasound via the skull.[74] This has been achieved using hundreds of transducers at very low frequency as a phased array, and clinical prototypes are available and under trial. To avoid unintended absorption and overheating of the scalp, a hemispherical phased array applicator with hundreds of elements operating at low frequency has been designed and successfully demonstrated within a small group of patients.[75] An alternative means of generating the ultrasound may provide a simplified means for inducing ultrasound within the brain and other deep-seated targets. Here the ultrasound generation is investigated from pulsed magnetic fields with the help of colloidal iron oxide nanoparticles. The advantage of ultrasound generated from magnetic fields is that the magnetic fields do not suffer the same attenuation as ultrasound through bones, soft tissue or air, and nanoparticles can be successfully delivered to various places in the human body. Recently, Hu et al.[69] have demonstrated that ultrasound can be generated via application of pulsed magnetic fields with the help of magnetic nanoparticles (mixture of Fe_2O_3 and Fe_3O_4). Hu et al. used the ultrasound for imaging purposes from the magnetic nanoparticles. Their work confirmed that ultrasound can be generated from the acceleration of magnetic nanoparticles in inhomogeneous magnetic fields. In a similar theoretical work, Carrey et al. have shown that the

effect is maximized and better controlled if a static magnetic field is superimposed on an alternating gradient.[76] Another important ultrasound generation mechanism in bulk magnetic materials is the magnetostriction effect.[77] Magnetostriction is a well-known effect of ferromagnetic materials to produce significant amount of strain when exposed to magnetic fields. The strain induced due to magnetic domain wall movement leads to significant amount of volume change, similar to the piezoelectric effect in ultrasonic transducers. The typical volume change of ferrous materials is on the order of 10^{-5}; e.g., the magnetostriction coefficients for Fe_3O_4 and γ-Fe_2O_3 are 1.6×10^{-5} and 0.7×10^{-5}, respectively.[78] This coefficient can be as high as 0.2% e.g. in Ni_2MnGa[79] and in $Tb_xDy_{1-x}Fe_2$.[80] Here, it is demonstrated that not only bulk materials, but also colloidal ferrofluids are capable of producing ultrasound. The ultrasound generated in this work is in agreement with the effect described by Hu et al.[69] They have shown that the ultrasound is generated in the inhomogeneous magnetic field; however, some ultrasound could also be observed as a result of the homogeneous magnetic field via the magnetostriction effect.

Detailed information about the construction of Helmholtz and anti-Helmholtz coils used in these experiments is presented in section 2.6 and 2.7.

5.2 Ultrasound Measurement from Strong Magnetic Pulses

In this study, the acoustic pressure generated from magnetic nanoparticles is investigated in the presence of pulsed magnetic fields. A glass capillary tube is filled with EMG 607 ferrofluid and exposed to homogeneous and inhomogeneous pulsed magnetic fields. Sound in the magnetic fluid is detected using a hydrophone integrated at the end of the glass capillary tube. Figure 25

shows the hydrophone signal in the presence of pulsed homogeneous magnetic fields when the dispersion of iron oxide nanoparticles is placed in the glass capillary tube. The distance of the detector from the pulse magnet is 6 in., and the concentration of the ferrofluid is 0.5 vol %. The graph also shows the current derivative signal from the magnetic field (as a reference) and the detected signal of the hydrophone in water in the absence of the nanoparticles. The signals are shifted for better visibility. Please note that there is no negative pressure present.
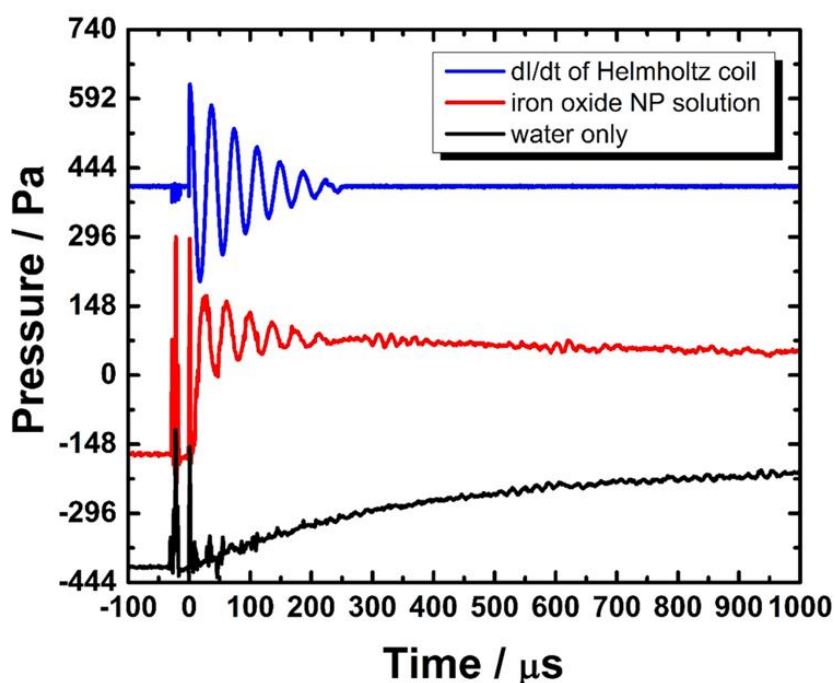
Figure 25 Detected ultrasonic signal from ferrofluid EMG 607 in homogeneous magnetic pulse with the current derivative signal from the magnetic field and the detected signal of the hydrophone in water in the absence of the nanoparticles. Reprinted with permission from ref.[48] Copyright (2016) American Chemical Society.

The initial pattern of the sound wave agrees well with the pattern observed from the pulsed magnetic field. When the tube is not filled with liquid, no appreciable amount of signal is observed from the pulsed magnetic fields, which rules out electrical interference from the driving circuit of the pulsed magnet. Notice that there is some signal detected from the water itself (see

also Figure 25) due to homogeneous strong pulsed magnetic fields, but no high frequency component is present. This is likely is due to some heating effects in the glass capillary tube and/or water itself. For the rest of the discussion, the water signal is subtracted from the ferrofluid signal to accurately gage the amount of high frequency sound generated from the nanoparticles.

The ultrasound from the nanoparticle dispersion exhibits strong concentration dependence. In order to accurately assess the amount of the ultrasound present, the time-domain signal is analyzed with Fourier analysis. The power coefficient of the concentration dependence is plotted against frequency, which shows a strong peak corresponding to the frequency of the magnetic field ($\sim$30 kHz) used in the experiment. This frequency component is missing from the water only sample, but it is present with increasing magnitude when the ferrofluid concentration is increased (Figure 26).
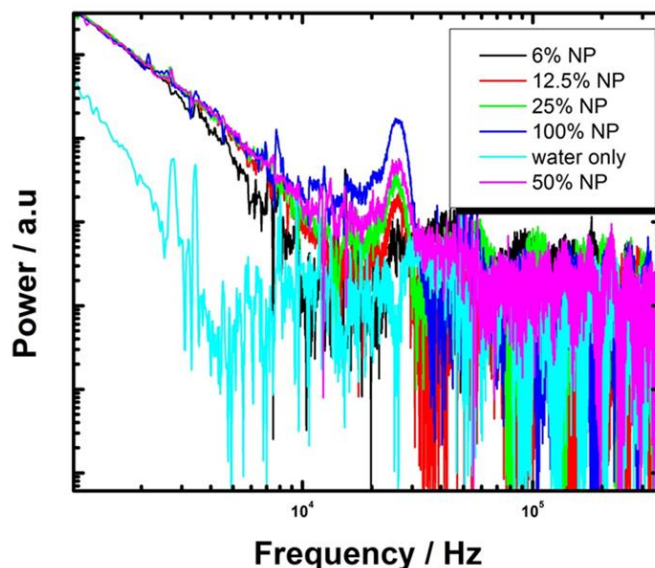
Figure 26 Fourier transform power spectrum of the detected ultrasonic signal from ferrofluid EMG 607 in homogeneous magnetic pulse. Reprinted with permission from ref.[48] Copyright (2016) American Chemical Society.

In Figure 26 is presented the Fourier transform power spectrum of the detected ultrasonic signal from ferrofluid EMG 607 in homogeneous magnetic pulse. The distance of the detector from the pulse magnet is 6 in. Increasing the concentration of the ferrofluid results in increased power coefficient at around 30 kHz. The power coefficient at 30 kHz in water is taken as the baseline signal. In addition to the main component of the signal at around 30 kHz, other low-frequency components are present, probably due to secondary effects such as heating from ultrasound and direct heating from the Brownian relaxation of magnetic nanoparticles.[81]

The ultrasonic signal was found to be inversely dependent with distance, with increasing amplitude of the 30 kHz component as the distance between and the magnet and the hydrophone was decreased. The attenuation of the ultrasonic signal is expected due to the loss of energy of sound waves and the organization of the ferrofluid.[82] Therefore, to accurately estimate the induced ultrasound signal, the ultrasonic signal is detected at various distances from the pulsed magnet. The ultrasound generated at zero distance is calculated from linear extrapolation of the distance dependent data (not shown). A comparison of the magnitude of ultrasound generated from inhomogeneous and homogeneous magnetic field is shown in Figure 27.
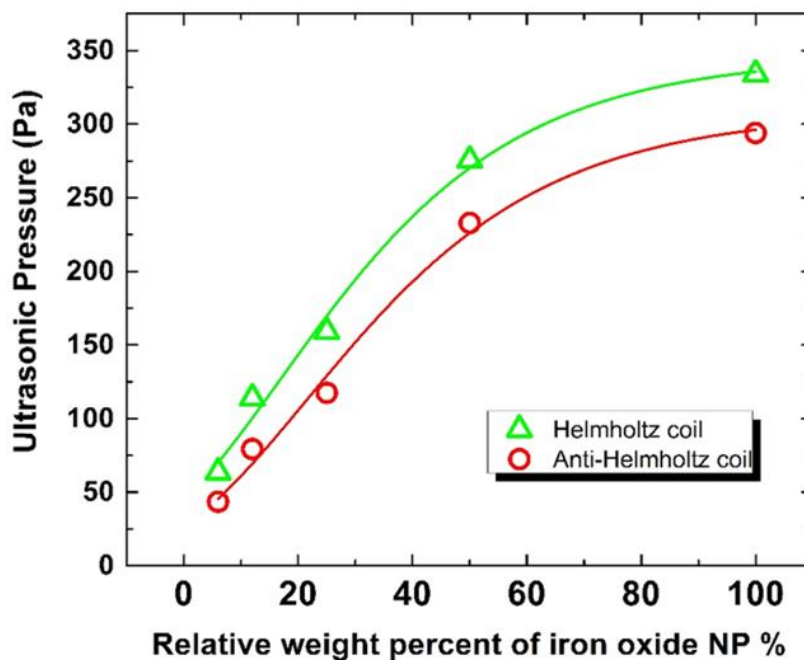
Figure 27 Comparison of the relative ultrasound generated from homogeneous and inhomogeneous magnetic field as a function of the ferrofluid concentrations. Reprinted with permission from ref.[48] Copyright (2016) American Chemical Society.

Surprisingly, the anti-Helmholtz coil generates less ultrasound pulse than the Helmholtz coil when the current in the coils are the same. Although the anti-Helmholtz coil has higher peak magnetic field gradient, it has lower average magnetic field gradient than the Helmholtz coil (Table 5-1).

	Pulsed coils		AC coils	
	Helmholtz	Anti-Helmholtz	Helmholtz	Anti-Helmholtz
Peak Magnetic field	15 T	5 T	2.7 mT	1.9 mT
Average Magnetic field	4.97 T	1.57 T	1.1 mT	0.7 mT

Peak Magnetic field gradient	321 T/m	475 T/m	0.138 T/m	0.221 T/m
Average Magnetic field gradient	0.173 T/m	0.168 T/m	0.049 T/m	0.064 T/m
Estimated Peak Force on 10 nm Particle	1.46×10^{-18} N	2.17×10^{-18} N	6.31×10^{-22} N	1.01×10^{-21} N
Estimated Average Force on 10 nm Particle	7.92×10^{-22} N	7.69×10^{-22} N	2.24×10^{-22} N	2.92×10^{-22} N
Measured max Pressure	334 Pa	294 Pa	10 Pa (at 200 kHz)	18 Pa (at 200 kHz)
Particle concentration	5.8×10^{15} NP/ml	5.8×10^{15} NP/ml	3.8×10^{16} NP/ml	3.8×10^{16} NP/ml
Measured force/particle	1.18×10^{-18} N	1.04×10^{-18} N	6.9×10^{-21} N	1.2×10^{-20} N

Table 5-1 Summary of the Calculated Coil Parameters, the Measured Pressure, and the Estimated and Measured Forces Acting on the EMG 607 Magnetic Nanoparticles. Reprinted with permission from ref.[48] Copyright (2016) American Chemical Society.

The data in Figure 27 also shows that the ultrasound pressure will decrease with increasing concentrations of nanoparticles, which could be the result of particle aggregation in external magnetic fields.[83] Consistent with this argument, it has been observed that in some of

the experiments after application of several magnetic pulses, the ferrofluid becomes destabilized and the particles in the dispersion are settled at the bottom of the tube.

5.3 Frequency-Dependent Ultrasound Measurements from Small Amplitude AC Magnetic Fields

In the second part of the experiment series, the frequency of the ultrasound is investigated at low magnetic field amplitude. The advantage of low magnetic field amplitude is the less likelihood of aggregation of the colloidal magnetic nanoparticles,[84] and the smaller amount of residual heating of the water itself as in the pulsed magnetic field experiments. Similar to the first part of the experiments, the ultrasound from colloidal magnetic nanoparticles is measured in two types of coils - in a Helmholtz coil and in an anti-Helmholtz coil – to assess the relative importance of the inhomogeneous and homogeneous magnetic fields on the colloidal dispersion of magnetic nanoparticles for ultrasound generation. The resulting data are shown in Figure 28.
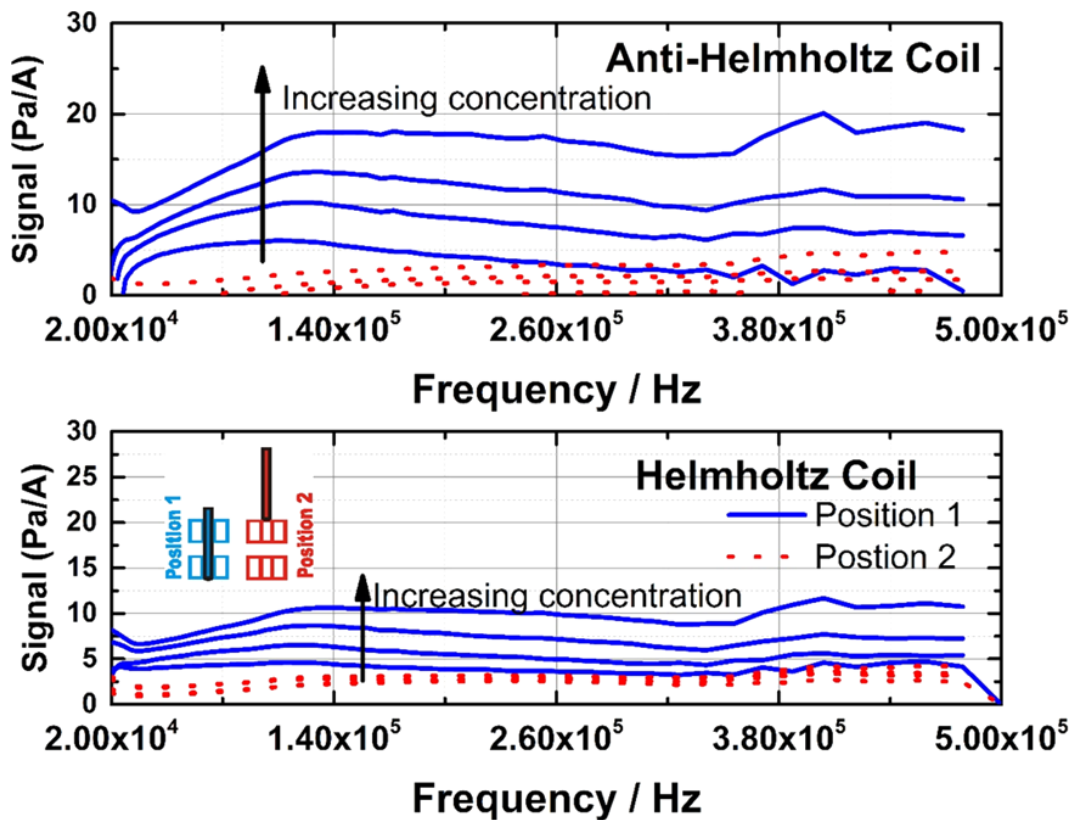
Figure 28 Frequency-dependent ultrasound from EMG 607 magnetic nanoparticle dispersion in homogeneous and inhomogeneous magnetic fields. The ultrasound pressure is normalized to the coil current to ensure that the ultrasound is compared at the same magnetic fields at all frequencies. Reprinted with permission from ref.[48] Copyright (2016) American Chemical Society.

As it can be seen in Figure 28, the anti-Helmholtz coil produce approximately twice the magnitude of ultrasound pressure as the Helmholtz coil. This strongly suggests that at these low magnetic field amplitudes the inhomogeneous magnetic field is key for the mechanism of ultrasound generation in EMG 607 magnetic dispersion. The figure also shows the data when the colloidal dispersion of magnetic nanoparticles is moved out of the magnets exhibiting minimal ultrasound generation. Interestingly, there is significant amount of ultrasound generated in both coils even at 500 kHz. The frequency dependence suggests that the ultrasound levels off as the frequency is increasing. Because in this experiment, the hydrophone is several inches away from

the ultrasound source, the frequency drop off the ultrasound is consistent with the attenuation of the ultrasound at higher frequencies. Based on these data, it is predicted that there is still significant ultrasound generated beyond 500 kHz frequencies.

5.4 Mechanism of ultrasound generation

There are two possible mechanisms for ultrasound generation in the ferrofluid. The first mechanism is the translational motion of the magnetic nanoparticles in the inhomogeneous magnetic fields as described by Hu et al.[69] The second mechanism is the magnetostriction effect (change of shape due to magnetization) of the magnetic nanoparticles in the homogeneous magnetic fields. This latter mechanism is well-known for the generation of ultrasound in the bulk. From these experiments the magnetostriction coefficient is calculated from the pulsed experiments by converting the voltage signal from the hydrophone to pressure using the sensitivity of the hydrophone. In order to accurately estimate the amount of ultrasound generated at the center of magnet, the initial ultrasound amplitude is extrapolated to the center of the magnet along with the error bars from the fit. The pressure is then converted to volume change from the known compressibility of the water (4.4×10^{-10} Pa^{-1}).[85] The calculated volume change is then normalized to the volume of the nanoparticles present in the magnetic field directly yielding the volume magnetostriction coefficient. The experiments use relatively large magnetic fields that ensures that the measurement is performed at magnetic fields where the iron oxide reaches its saturation magnetization. As shown in Figure 29, the calculated magnetostriction coefficient is comparable to the bulk magnetostriction coefficient of iron oxide; however, the magnetostriction coefficient is somewhat larger magnitude than the bulk magnetostriction coefficient of bulk iron oxide.
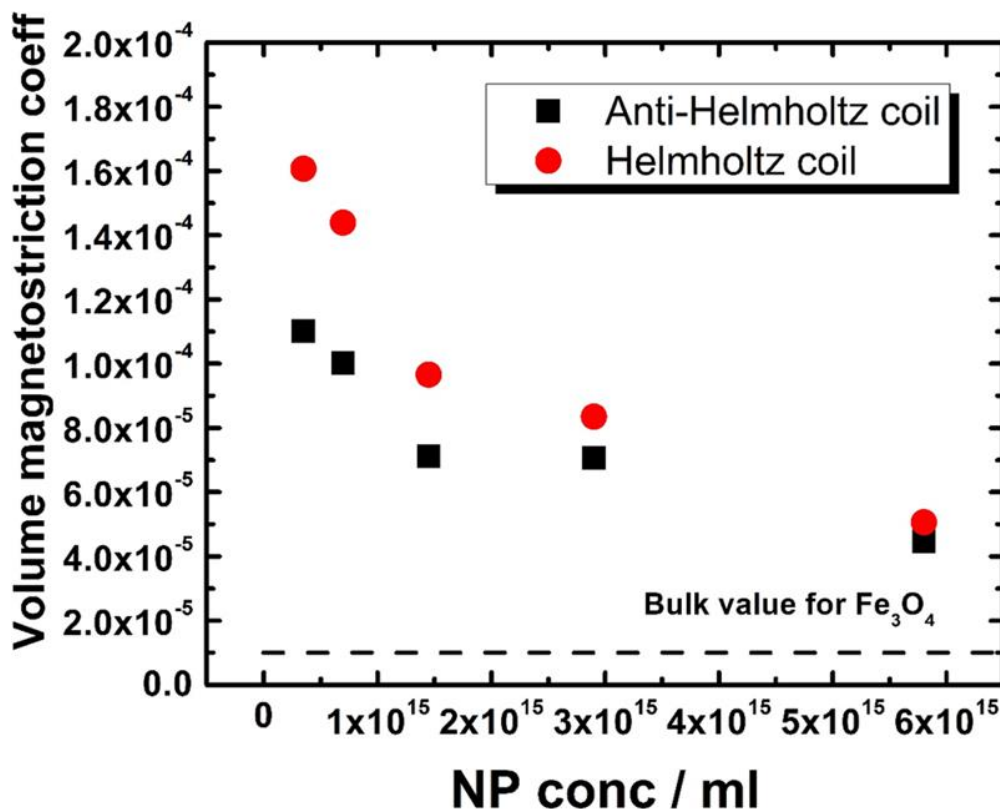
Figure 29 Calculated volume magnetostriction coefficient of iron oxide particles from the compressibility of water (4.6×10^{-10} Pa^{-1}) as a function of nanoparticle concentration. The bulk magnetostriction coefficient of iron oxide is also indicated in the graph by the dashed line. Reprinted with permission from ref.[48] Copyright (2016) American Chemical Society.

In addition, the magnetostriction coefficient shows a concentration dependence. These

experiments show an inverse relationship between the nanoparticle concentrations vs the

magnetostriction coefficient for iron oxide. At higher concentration of the ferrofluid, the

response becomes more bulklike. The deviation of the magnetostriction coefficient especially at

lower concentrations becomes significant. We hypothesize that the difference between the

observed magnetostriction coefficient and the magnetostriction coefficient calculated from the

experiments has to come from a different mechanism. We propose that at lower concentration of

the colloidal dispersion of magnetic nanoparticles the particles are less confined to move around,

and ultrasound generation from the translation motion of the magnetic particles becomes more

effective. This additional motion of the particles in the magnetic field gradient becomes dominant under these conditions for ultrasound generation.

The translational displacement of the magnetic nanoparticles in the presence of inhomogeneous magnetic fields is primarily controlled by the presence of magnetic field gradient and the magnetic field. According to Cao et al.,[86] the magnetic force ($\vec{F}_m$) that a spherical particle experiences in a colloidal dispersion, after reaching terminal speed due to solvent drag forces, can be divided into two regions. At low magnetic fields, when $\overrightarrow{H_a} < \frac{\chi+3}{3\chi}\overrightarrow{M_{sat}}$, and $\overrightarrow{F_m} = \frac{V_m}{\mu_0}\frac{3\chi}{\chi+3}(\overrightarrow{H_a}\nabla)\overrightarrow{H_a}$, where μ_0 is the vacuum permeability, V_m is the particle volume, χ is the magnetic susceptibility, M_{sat} is the saturation magnetization, and H_a is the magnetic field. At high magnetic fields, $\overrightarrow{F_m} = \frac{V_m}{\mu_0}(\overrightarrow{M_{sat}}\nabla)\overrightarrow{H_a}$ when $\overrightarrow{H_a} \geq \frac{\chi+3}{3\chi}\overrightarrow{M_{sat}}$. The EMG 607 colloidal solution has a saturation magnetization at 11 mT. This low saturation magnetization strongly suggests that in the strong pulsed magnetic field experiments the magnetic force (pressure) produced from the inhomogeneous magnetic field will be linearly proportional to the external magnetic field. As shown in Figure 30, in the pulsed experiments the pressure is directly proportional to the magnetic field.
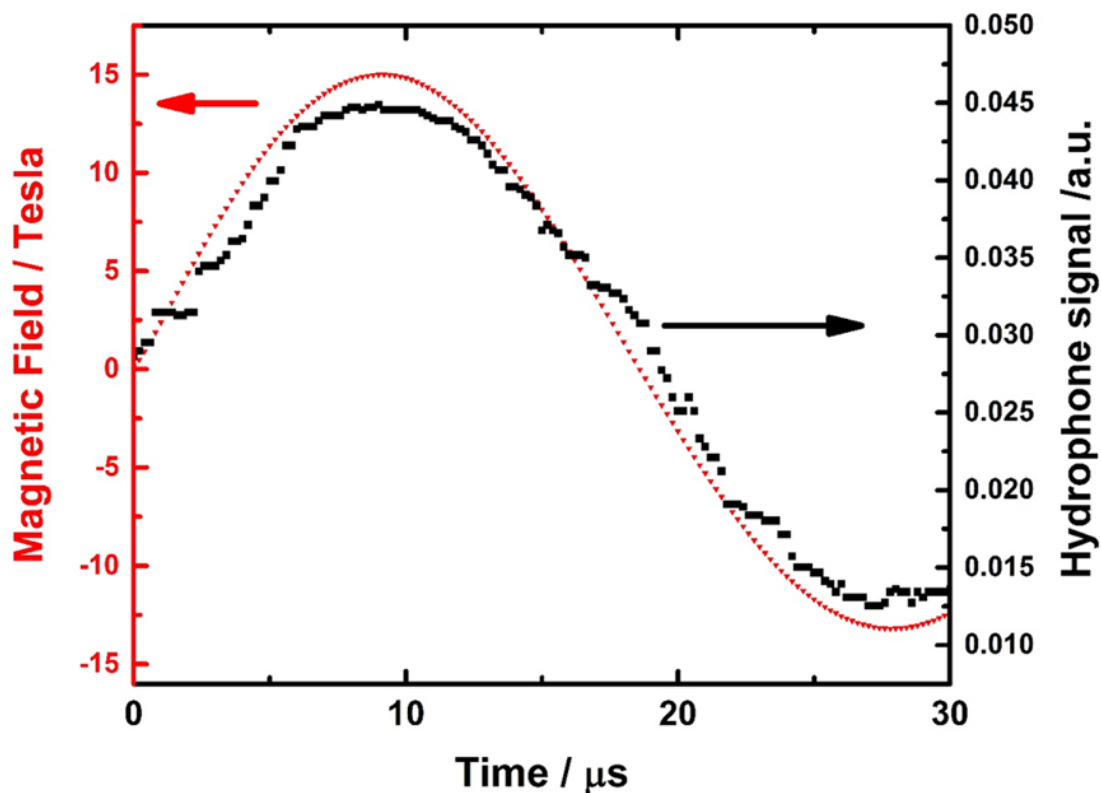
Figure 30 Comparison of the magnetic field and the pressure signal in the Helmholtz coil. Similar results can be obtained for the anti-Helmholtz coil. The result shows that the induced pressure is directly proportional to the magnetic field in this case. Reprinted with permission from ref.[48] Copyright (2016) American Chemical Society.

In the AC experiments (Figure 31), our calculation shows that the magnetic field is between 2 and 3 mT, which is comparable to, but less than, the saturation magnetization; however, due to the strong decrease of the susceptibility of the colloidal magnetic particles at higher frequencies, we expect to observe that the pressure will be linearly proportional to the magnetic field.
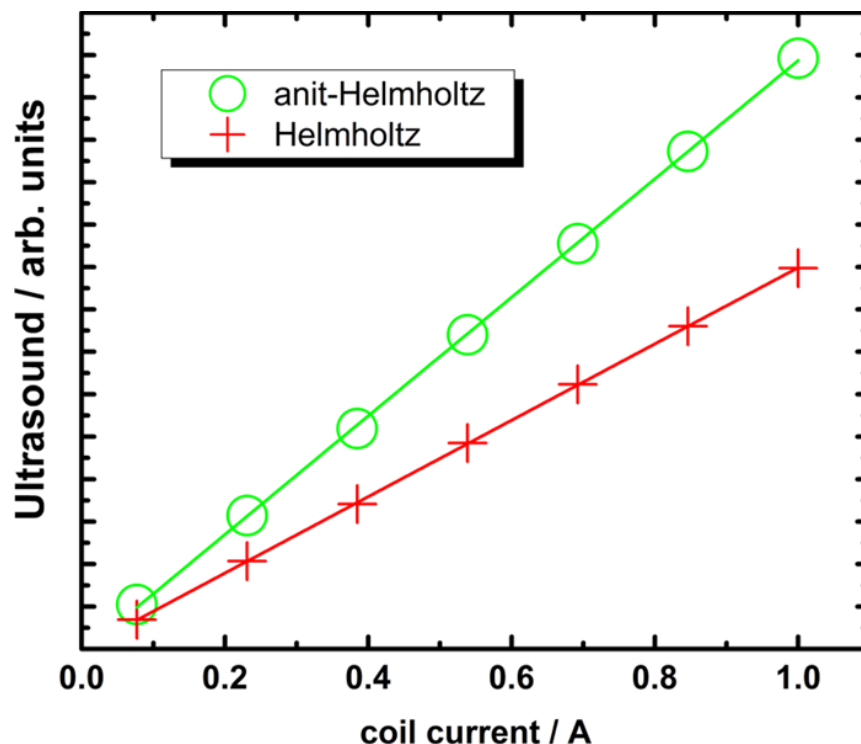
Figure 31 Dependence of ultrasound at 200 kHz on coil current from EMG 607 magnetic nanoparticle dispersion in two different coils in the frequency-dependent ultrasound measurements. Reprinted with permission from ref.[48] Copyright (2016) American Chemical Society.

As shown in Figure 31, the pressure signal from the ultrasonic sensor is also linear with respect to the coil current (magnetic field). The spherical magnetic nanoparticle will experience a force in the direction of the magnetic field gradient. It is important to point out that both the Helmholtz coil and the anti-Helmholtz coil produce a significant amount of magnetic field gradients. Table 5-1 summarizes the calculated and measured forces in these experiments. The force that the hydrophone experiences is the result of the pressure wave produced in different parts of the colloidal dispersion inside the coils. Forces estimated based on both the peak magnetic field gradient and the average magnetic field gradient of the particles in the magnetic coil are shown in Table 5-1. The measured forces/magnetic particles are calculated from the experimentally measured ultrasonic pressures. The data show that the pressure calculated from

experiments agrees very well with the estimated pressures expected based on the available magnetic field gradient. The estimated force is comparable to the values listed in the literature for a similar sized magnetic nanoparticles.[76] There are several biocompatible colloidal nanoparticle systems that are already being utilized for magnetic hyperthermia treatments.[54b] Modifying these nanoparticles systems to produce ultrasound for various purposes will be a simple modification of the type of magnetic field generators used to reach to higher magnetic fields. Nonthermal effects of ultrasound include cavitation, which is employed for delivery of drugs and other small molecules to cells.[87] The threshold for inducing cavitation required for adjusting membrane permeability is on the order of ~450 kPa;[88] this threshold may be reduced in the presence of microbubbles and other cavitation nuclei. Other nonthermal bioeffects of low intensity ultrasound may be achieved at lower intensities. With greater driving current, the acoustic intensities generated by the proposed technique have application for localized modification of the permeability of cell membranes for delivery of therapeutic agents and stimulating bioeffects. We anticipate that the ultrasound from magnetic nanoparticles will be able to effectively manipulate the permeability of small molecules across lipid bilayers.[89]

5.5 Conclusion

In this chapter, the ultrasound is detected from the pulsed magnetic from colloidal magnetic nanoparticles. Comparison of the data from homogeneous and inhomogeneous magnetic fields suggests that the ultrasound is driven primarily by the presence of the inhomogeneous magnetic fields.

Chapter 6 - Summary

In summary, this thesis presented the latest advancements in drug delivery systems, (including its underlying mechanics) while focusing on attaining drug release from magneto liposomes upon exposure to pulsed magnetic field.

Magneto liposomes are studied as a drug delivery platform, including the synthesis of paramagnetic nanoparticles and magneto liposomes. Upon confirming drug release from magneto liposomes, several potential applications arise including: (1) Instantaneous delivery of drugs with both temporal and special precision. (2) Delivery of therapeutic agents for cancer therapy. (3) Delivery of pain killer drug locally following the injection of the drug loaded into magneto liposomes via intravenous therapy. (4) Experimental tool to induce instant repeated physiological changes from drugs, therefore allowing kinetic studies in living systems. (5) Manipulating/modulating cellular permeability via mechanical force from the pulsed magnetic fields.

In addition, the construction and operation of a novel Helmholtz are demonstrated to generate strong rotating magnetic field. The design shows scalability by manipulating several factors: increasing the number of plates used to construct the coils, reducing its dimensions, and increasing discharge voltage.

Finally, the ultrasound is detected from the pulsed magnetic from colloidal magnetic nanoparticles. Comparison of the data from homogeneous and inhomogeneous magnetic fields suggests that the ultrasound is driven primarily by the presence of the inhomogeneous magnetic fields. Confirming that ultrasound is generated from colloidal paramagnetic nanoparticles, will

have applications toward the acoustic induction of bioeffects in cells and manipulating the permeability of biological membranes.

Although attaining drug release from magneto liposomes upon exposure to pulsed magnetic fields has been successful, several improvements can be made: (1) relocating the magnetic nanoparticles outside of the liposomes using a chemical linker. Since ultrasounds are produced from magnetic nanoparticles, relocating the magnetic nanoparticles outside of the liposome can reduce the complexity of the protocol for synthesis of liposomes. In the same time, the interior of the liposome will be "available", for a larger amount of drug to be incorporated. In addition, placing the magnetic nanoparticles outside the liposomes will result in less aggregation and a higher number of nanoparticles available per liposome. (2) Improving magnetic nanoparticle functionality with gold. Iron oxide gold coated nanoparticles will significantly improve the versatility of the magneto liposome systems by providing a solid and well-studied platform to bind ligands to the nanoparticles. In addition, a recent study,[90] proves that, when cytotoxicity of HepG2 malignant tumor cells is assessed, gold coated iron oxide nanoparticles show 52% less toxicity compared to iron oxide nanoparticles.

References

1.   Akhtar, N.; Khan, R. A., Liposomal systems as viable drug delivery technology for skin cancer sites with an outlook on lipid-based delivery vehicles and diagnostic imaging inputs for skin conditions. *Prog Lipid Res* **2016,** *64*, 192-230.

2.   Zhao, M.; Ding, X. F.; Shen, J. Y.; Zhang, X. P.; Ding, X. W.; Xu, B., Use of liposomal doxorubicin for adjuvant chemotherapy of breast cancer in clinical practice. *J Zhejiang Univ-Sc B* **2017,** *18* (1), 15-26.

3.   Mahmud, M.; Piwoni, A.; Filiczak, N.; Janicka, M.; Gubernator, J., Long-Circulating Curcumin-Loaded Liposome Formulations with High Incorporation Efficiency, Stability and Anticancer Activity towards Pancreatic Adenocarcinoma Cell Lines In Vitro. *Plos One* **2016,** *11* (12).

4.   Çağdaş, M.; Sezer, A. D.; Bucak, S., *Liposomes as Potential Drug Carrier Systems for Drug Delivery*. 2014.

5.   Buboltz, J. T.; Feigenson, G. W., A novel strategy for the preparation of liposomes: rapid solvent exchange. *Bba-Biomembranes* **1999,** *1417* (2), 232-245.

6.   Langer, R., Drug delivery and targeting. *Nature* **1998,** *392* (6679), 5-10.

7.   Slingerland, M.; Guchelaar, H. J.; Gelderblom, H., Liposomal drug formulations in cancer therapy: 15 years along the road. *Drug Discov Today* **2012,** *17* (3-4), 160-166.

8.   Nobuto, H.; Sugita, T.; Kubo, T.; Shimose, S.; Yasunaga, Y.; Murakami, T.; Ochi, M., Evaluation of systemic chemotherapy with magnetic liposomal doxorubicin and a dipole external electromagnet. *Int J Cancer* **2004,** *109* (4), 627-635.

9.   Schafer, F. Q.; Buettner, G. R., Redox environment of the cell as viewed through the redox state of the glutathione disulfide/glutathione couple. *Free Radical Bio Med* **2001,** *30* (11), 1191-1212.

10.   Ahmed, S. E.; Martins, A. M.; Husseini, G. A., The use of ultrasound to release chemotherapeutic drugs from micelles and liposomes. *J Drug Target* **2015,** *23* (1), 16-42.

11.   Javadi, M.; Pitt, W. G.; Belnap, D. M.; Tsosie, N. H.; Hartley, J. M., Encapsulating Nanoemulsions Inside eLiposomes for Ultrasonic Drug Delivery. *Langmuir* **2012,** *28* (41), 14720-14729.

12.   Arias, J. L., Drug Targeting Strategies in Cancer Treatment: An Overview. *Mini-Rev Med Chem* **2011,** *11* (1), 1-17.

13.   Zhu, L.; Kate, P.; Torchilin, V. P., Matrix Metalloprotease 2-Responsive Multifunctional Liposomal Nanocarrier for Enhanced Tumor Targeting. *Acs Nano* **2012,** *6* (4), 3491-3498.

14.   Weijer, R.; Broekgaarden, M.; Kos, M.; van Vught, R.; Rauws, E. A. J.; Breukink, E.; van Gulik, T. M.; Storm, G.; Heger, M., Enhancing photodynamic therapy of refractory solid cancers: Combining second-generation photosensitizers with multi-targeted liposomal delivery. *J Photoch Photobio C* **2015,** *23*, 103-131.

15.   Vahed, S. Z.; Salehi, R.; Davaran, S.; Sharifi, S., Liposome-based drug co-delivery systems in cancer cells. *Mat Sci Eng C-Mater* **2017,** *71*, 1327-1341.

16.   Sharifi, S.; Barar, J.; Hejazi, M. S.; Samadi, N., Doxorubicin Changes Bax /Bcl-xLRatio, Caspase-8 and 9 in Breast Cancer Cells. *Advanced Pharmaceutical Bulletin 5* (3), 351-359.

17.   BASEL, M. T., TARGETING CANCER THERAPY: USING PROTEASE CLEAVAGE SEQUENCES TO DEVELOP MORE SELECTIVE AND EFFECTIVE CANCER TREATMENTS. **2010**.

18.   Torchilin, V. P., Multifunctional nanocarriers. *Adv Drug Deliver Rev* **2012,** *64*, 302-315.

19.   Kumar, A.; Zhang, X.; Liang, X. J., Gold nanoparticles: Emerging paradigm for targeted drug delivery system. *Biotechnol Adv* **2013,** *31* (5), 593-606.

20.   Zhang, X. A.; Chibli, H.; Mielke, R.; Nadeau, J., Ultrasmall Gold-Doxorubicin Conjugates Rapidly Kill Apoptosis-Resistant Cancer Cells. *Bioconjugate Chem* **2011,** *22* (2), 235-243.

21.   Duncan, R.; Sat, Y. N., Tumour targeting by enhanced permeability and retention (EPR) effect. *Ann Oncol* **1998,** *9*, 39-39.

22.   del Rosal, B.; Perez-Delgado, A.; Carrasco, E.; Jovanovic, D. J.; Dramicanin, M. D.; Drazic, G.; de la Fuente, A. J.; Sanz-Rodriguez, F.; Jaque, D., Neodymium-Based Stoichiometric Ultrasmall Nanoparticles for Multifunctional Deep-Tissue Photothermal Therapy. *Adv Opt Mater* **2016,** *4* (5), 782-789.

23.   Ahamed, M.; Akhtar, M. J.; Alhadlaq, H. A.; Alshamsan, A., Copper ferrite nanoparticle-induced cytotoxicity and oxidative stress in human breast cancer MCF-7 cells. *Colloid Surface B* **2016,** *142*, 46-54.

24.   Fontana, F.; Liu, D. F.; Hirvonen, J.; Santos, H. A., Delivery of therapeutics with nanoparticles: what's new in cancer immunotherapy? *Wires Nanomed Nanobi* **2017,** *9* (1).

25.   Hansen, A. H.; Mouritsen, O. G.; Arouri, A., Enzymatic action of phospholipase A(2) on liposomal drug delivery systems. *Int J Pharmaceut* **2015,** *491* (1-2), 49-57.

26.   (a) Belinsky, G. S.; Rajan, T. V.; Saria, E. A.; Giardina, C.; Rosenberg, D. W., Expression of secretory phospholipase A2 in colon tumor cells potentiates tumor growth. *Mol Carcinogen* **2007,** *46* (2), 106-116; (b) Burke, J. E.; Dennis, E. A., Phospholipase A(2) structure/function, mechanism, and signaling. *J Lipid Res* **2009,** *50*, S237-S242.

27.   Scott, K. F.; Sajinovic, M.; Hein, J.; Nixdorf, S.; Galettis, P.; Liauw, W.; de Souza, P.; Dong, Q. H.; Graham, G. G.; Russell, P. J., Emerging roles for phospholipase A(2) enzymes in cancer. *Biochimie* **2010,** *92* (6), 601-610.

28.   Andresen, T. L.; Jensen, S. S.; Jorgensen, K., Advanced strategies in liposomal cancer therapy: Problems and prospects of active and tumor specific drug release. *Prog Lipid Res* **2005,** *44* (1), 68-97.

29.   Lajunen, T.; Nurmi, R.; Kontturi, L.; Viitala, L.; Yliperttula, M.; Murtomaki, L.; Urtti, A., Light activated liposomes: Functionality and prospects in ocular drug delivery. *J Control Release* **2016,** *244*, 157-166.

30.   Timko, B. P.; Dvir, T.; Kohane, D. S., Remotely Triggerable Drug Delivery Systems. *Adv Mater* **2010,** *22* (44), 4925-4943.

31.   (a) Lajunen, T.; Viitala, L.; Kontturi, L. S.; Laaksonen, T.; Liang, H. M.; Vuorimaa-Laukkanen, E.; Viitala, T.; Le Guevel, X.; Yliperttula, M.; Murtomaki, L.; Urtti, A., Light induced cytosolic drug delivery from liposomes with gold nanoparticles. *J Control Release* **2015,** *203*, 85-98; (b) Kautzka, Z.; Clement, S.; Goldys, E. M.; Deng, W., Light-triggered liposomal cargo delivery platform incorporating photosensitizers and gold nanoparticles for enhanced singlet oxygen generation and increased cytotoxicity. *Int J Nanomed* **2017,** *12*, 969-977.

32.   Boissenot, T.; Bordat, A.; Fattal, E.; Tsapis, N., Ultrasound-triggered drug delivery for cancer treatment using drug delivery systems: From theoretical considerations to practical applications. *J Control Release* **2016,** *241*, 144-163.

33.   Mitragotri, S., Innovation - Healing sound: the use of ultrasound in drug delivery and other therapeutic applications. *Nat Rev Drug Discov* **2005,** *4* (3), 255-260.

34.   Liu, Y. Y.; Miyoshi, H.; Nakamura, M., Encapsulated ultrasound microbubbles: Therapeutic application in drug/gene delivery. *J Control Release* **2006,** *114* (1), 89-99.

35.   Zhu, F. Y.; Jiang, Y.; Luo, F.; Li, P., Effectiveness of localized ultrasound-targeted microbubble destruction with doxorubicin liposomes in H22 mouse hepatocellular carcinoma model. *J Drug Target* **2015,** *23* (4), 323-334.

36.   Myhr, G.; Moan, J., Synergistic and tumour selective effects of chemotherapy and ultrasound treatment. *Cancer Lett* **2006,** *232* (2), 206-213.

37.   (a) Moses, M. A.; Brem, H.; Langer, R., Advancing the field of drug delivery: Taking aim at cancer. *Cancer Cell* **2003,** *4* (5), 337-341; (b) Allen, T. M.; Cullis, P. R., Drug delivery systems: Entering the mainstream. *Science* **2004,** *303* (5665), 1818-1822.

38.   Basel, M. T.; Balivada, S.; Wang, H. W.; Shrestha, T. B.; Seo, G. M.; Pyle, M.; Abayaweera, G.; Dani, R.; Koper, O. B.; Tamura, M.; Chikan, V.; Bossmann, S. H.; Troyer, D. L., Cell-delivered magnetic nanoparticles caused hyperthermia-mediated increased survival in a murine pancreatic cancer model. *Int J Nanomed* **2012,** *7*, 297-306.

39.   Podaru, G.; Ogden, S.; Baxter, A.; Shrestha, T.; Ren, S.; Thapa, P.; Dani, R. K.; Wang, H.; Basel, M. T.; Prakash, P.; Bossmann, S. H.; Chikan, V., Pulsed Magnetic Field Induced Fast Drug Release from Magneto Liposomes via Ultrasound Generation. *The Journal of Physical Chemistry B* **2014,** *118* (40), 11715-11722.

40.   (a) Sparreboom, A.; Kehrer, D. F. S.; Mathijssen, R. H. J.; Xie, R.; de Jonge, M. J. A.; de Bruijn, P.; Planting, T.; Eskens, F. A. L. M.; Verheij, C.; de Heus, G.; Klaren, A.; Zhang, S.; Verhaeghe, T.; Palmer, P. A.; Verweij, J., Phase I and pharmacokinetic study of irinotecan in combination with R115777, a farnesyl protein transferase inhibitor. *Brit J Cancer* **2004,** *90* (8), 1508-1515; (b) Rozners, E.; Tanui, P.; Selvam, C.; Kennedy, S. D.; Mutisya, D.; Lunstad, B. D.; Leake, D., Synthesis and properties of non-ionic RNA analogs for applications in RNA interference. *Abstr Pap Am Chem S* **2013,** *246*.

41.   Nappini, S.; Bonini, M.; Ridi, F.; Baglioni, P., Structure and permeability of magnetoliposomes loaded with hydrophobic magnetic nanoparticles in the presence of a low frequency magnetic field. *Soft Matter* **2011,** *7* (10), 4801-4811.

42.   Wang, C.; Hou, Y. L.; Kim, J. M.; Sun, S. H., A general strategy for synthesizing FePt nanowires and nanorods. *Angew Chem Int Edit* **2007,** *46* (33), 6333-6335.

43.   Lacroix, L. M.; Huls, N. F.; Ho, D.; Sun, X. L.; Cheng, K.; Sun, S. H., Stable Single-Crystalline Body Centered Cubic Fe Nanoparticles. *Nano Lett* **2011,** *11* (4), 1641-1645.

44.   Herlach, F., Pulsed magnets. *Rep Prog Phys* **1999,** *62* (6), 859-920.

45.   Bartkevicius, S.; Novickij, J., The Investigation of Magnetic Field Distribution of Dual Coil Pulsed Magnet. *Elektron Elektrotech* **2009,** (4), 23-26.

46.   Salaoru, T. A.; Woodward, J. R., Rapid rise time pulsed magnetic field circuit for pump-probe field effect studies. *Rev Sci Instrum* **2007,** *78* (3).

47.   Mackay, K.; Bonfim, M.; Givord, D.; Fontaine, A., 50 T pulsed magnetic fields in microcoils. *J Appl Phys* **2000,** *87* (4), 1996-2002.

48.   Podaru, G. V.; Chikan, V., Magnetic Field Induced Ultrasound from Colloidal Superparamagnetic Nanoparticles. *J Phys Chem C* **2016,** *120* (4), 2386-2391.

49.   Jordan, A.; Scholz, R.; Wust, P.; Fahling, H.; Felix, R., Magnetic fluid hyperthermia (MFH): Cancer treatment with AC magnetic field induced excitation of biocompatible superparamagnetic nanoparticles. *J Magn Magn Mater* **1999,** *201*, 413-419.

50.   Wernsdorfer, W.; Orozco, E. B.; Hasselbach, K.; Benoit, A.; Barbara, B.; Demoncy, N.; Loiseau, A.; Pascard, H.; Mailly, D., Experimental evidence of the Neel-Brown model of magnetization reversal. *Phys Rev Lett* **1997,** *78* (9), 1791-1794.

51.   (a) Mornet, S.; Vasseur, S.; Grasset, F.; Duguet, E., Magnetic nanoparticle design for medical diagnosis and therapy. *J Mater Chem* **2004,** *14* (14), 2161-2175; (b) Duguet, E.; Vasseur, S.; Mornet, S.; Devoisselle, J. M., Magnetic nanoparticles and their applications in medicine. *Nanomedicine-Uk* **2006,** *1* (2), 157-168.

52.   Lee, J. H.; Jang, J. T.; Choi, J. S.; Moon, S. H.; Noh, S. H.; Kim, J. W.; Kim, J. G.; Kim, I. S.; Park, K. I.; Cheon, J., Exchange-coupled magnetic nanoparticles for efficient heat induction. *Nat Nanotechnol* **2011,** *6* (7), 418-422.

53.   (a) Sharapova, V. A.; Uimin, M. A.; Mysik, A. A.; Ermakov, A. E., Heat Release in Magnetic Nanoparticles in AC Magnetic Fields. *Phys Met Metallogr+* **2010,** *110* (1), 5-12; (b) Raikher, Y. L.; Stepanov, V. I., Energy absorption by a magnetic nanoparticle suspension in a rotating field. *J Exp Theor Phys+* **2011,** *112* (1), 173-177.

54.   (a) Wang, H. W.; Shrestha, T. B.; Basel, M. T.; Dani, R. K.; Seo, G. M.; Balivada, S.; Pyle, M. M.; Prock, H.; Koper, O. B.; Thapa, P. S.; Moore, D.; Li, P.; Chikan, V.; Troyer, D. L.; Bossmann, S. H., Magnetic-Fe/Fe3O4-nanoparticle-bound SN38 as carboxylesterase-cleavable prodrug for the delivery to tumors within monocytes/macrophages. *Beilstein J Nanotech* **2012,** *3*, 444-455; (b) Rachakatla, R. S.; Balivada, S.; Seo, G. M.; Myers, C. B.; Wang, H. W.; Samarakoon, T. N.; Dani, R.; Pyle, M.; Kroh, F. O.; Walker, B.; Leaym, X. X.; Koper, O. B.; Chikan, V.; Bossmann, S. H.; Tamura, M.; Troyer, D. L., Attenuation of Mouse Melanoma by A/C Magnetic Field after Delivery of Bi-Magnetic Nanoparticles by Neural Progenitor Cells. *Acs Nano* **2010,** *4* (12), 7093-7104.

55.   Rinaldi, C.; Gutman, F.; He, X. W.; Rosenthal, A. D.; Zahn, M., Torque measurements on ferrofluid cylinders in rotating magnetic fields. *J Magn Magn Mater* **2005,** *289*, 307-310.

56.   Tomasini, M. D.; Rinaldi, C.; Tomassone, M. S., Molecular dynamics simulations of rupture in lipid bilayers. *Exp Biol Med* **2010,** *235* (2), 181-188.

57.   Suresh, S., Biomechanics and biophysics of cancer cells. *Acta Biomater* **2007,** *3* (4), 413-438.

58.   Bitter, F., New Developments in High-Magnetic-Field Research. *Phys Today* **1961,** *14* (9), 22-28.

59.   Podaru, G.; Moore, J.; Dani, R. K.; Prakash, P.; Chikan, V., Nested Helmholtz coil design for producing homogeneous transient rotating magnetic fields. *Rev Sci Instrum* **2015,** *86* (3).

60.   Waring, C. E.; Custer, R. L., Absolute Verdet Constants for Water over a Range of Temperatures and Visible Wave Lengths. *J Am Chem Soc* **1952,** *74* (10), 2506-2509.

61.   Small, L. L.; Mcken, D. C. D.; Offenberger, A. A., Low-Jitter, Low-Inductance, Electrically Triggered Spark Gap. *Rev Sci Instrum* **1984,** *55* (7), 1084-1089.

62.   Bangham, A. D.; Horne, R. W., Negative Staining of Phospholipids + Their Structural Modification by-Surface Active Agents as Observed in Electron Microscope. *J Mol Biol* **1964,** *8* (5), 660-&.

63.   Bangham, A. D.; Hill, M. W.; Miller, N. G. A., Preparation and Use of Liposomes as Models of Biological Membranes. In *Methods in Membrane Biology: Volume 1*, Korn, E. D., Ed. Springer US: Boston, MA, 1974; pp 1-68.

64.   (a) Gregoriadis, G.; Ryman, B. E., Fate of Protein-Containing Liposomes Injected into Rats. *European Journal of Biochemistry* **1972,** *24* (3), 485-491; (b) Pandey, H.; Rani, R.; Agarwal, V., Liposome and Their Applications in Cancer Therapy. *Brazilian Archives of Biology and Technology* **2016,** *59*.

65.   Fenske, D. B.; Cullis, P. R., Entrapment of small molecules and nucleic acid-based drugs in liposomes. *Method Enzymol* **2005,** *391*, 7-40.

66.	Guven, A.; Ortiz, M.; Constanti, M.; O'Sullivan, C. K., Rapid and efficient method for the size separation of homogeneous fluorescein-encapsulating liposomes. *J Liposome Res* **2009,** *19* (2), 148-154.

67.	Lasic, D. D.; Martin, F. J.; Gabizon, A.; Huang, S. K.; Papahadjopoulos, D., Sterically Stabilized Liposomes - a Hypothesis on the Molecular-Origin of the Extended Circulation Times. *Biochim Biophys Acta* **1991,** *1070* (1), 187-192.

68.	Weissig, V.; Boddapati, S. V.; Cheng, S. M.; D'Souza, G. G. M., Liposomes and liposome-like vesicles for drug and DNA delivery to mitochondria. *J Liposome Res* **2006,** *16* (3), 249-264.

69.	Hu, G.; He, B., Magnetoacoustic imaging of magnetic iron oxide nanoparticles embedded in biological tissues with microsecond magnetic stimulation. *Appl Phys Lett* **2012,** *100* (1).

70.	(a) Dromi, S.; Frenkel, V.; Luk, A.; Traughber, B.; Angstadt, M.; Bur, M.; Poff, J.; Xie, J. W.; Libutti, S. K.; Li, K. C. P.; Wood, B. J., Pulsed-high intensity focused ultrasound and low temperature sensitive liposomes for enhanced targeted drug delivery and antitumor effect. *Clin Cancer Res* **2007,** *13* (9), 2722-2727; (b) Huang, S. L.; MacDonald, R. C., Acoustically active liposomes for drug encapsulation and ultrasound-triggered release. *Bba-Biomembranes* **2004,** *1665* (1-2), 134-141; (c) Schroeder, A.; Kost, J.; Barenholz, Y., Ultrasound, liposomes, and drug delivery: principles for using ultrasound to control the release of drugs from liposomes. *Chem Phys Lipids* **2009,** *162* (1-2), 1-16.

71.	Taketomi, S.; Ogawa, S.; Miyajima, H.; Chikazumi, S.; Nakao, K.; Sakakibara, T.; Goto, T.; Miura, N., Dynamical Properties of Magneto-Optical Effect in Magnetic Fluid Thin-Films. *J Appl Phys* **1988,** *64* (10), 5846-5848.

72.	(a) Cutillas, S.; Liu, J., Experimental study on the fluctuations of dipolar chains. *Phys Rev E* **2001,** *64* (1); (b) Promislow, J. H. E.; Gast, A. P., Magnetorheological fluid structure in a pulsed magnetic field. *Langmuir* **1996,** *12* (17), 4095-4102.

73.	Kinoshita, M.; McDannold, N.; Jolesz, F. A.; Hynynen, K., Noninvasive localized delivery of Herceptin to the mouse brain by MRI-guided focused ultrasound-induced blood-brain barrier disruption. *P Natl Acad Sci USA* **2006,** *103* (31), 11719-11723.

74.	Xie, F.; Boska, M. D.; Lof, J.; Uberti, M. G.; Tsutsui, J. M.; Porter, T. R., Effects of Transcranial Ultrasound and Intravenous Microbubbles on Blood Brain Barrier Permeability in a Large Animal Model. *Ultrasound Med Biol* **2008,** *34* (12), 2028-2034.

75.	McDannold, N.; Clement, G. T.; Black, P.; Jolesz, F.; Hynynen, K., Transcranial Magnetic Resonance Imaging-Guided Focused Ultrasound Surgery of Brain Tumors: Initial Findings in 3 Patients. *Neurosurgery* **2010,** *66* (2), 323-332.

76.	Carrey, J.; Connord, V.; Respaud, M., Ultrasound generation and high-frequency motion of magnetic nanoparticles in an alternating magnetic field: Toward intracellular ultrasound therapy? *Appl Phys Lett* **2013,** *102* (23).

77.	(a) Callen, E.; Callen, H. B., Magnetostriction Forced Magnetostriction and Anomalous Thermal Expansion in Ferromagnets. *Phys Rev* **1965,** *139* (2A), A455-&; (b) James, R. D.; Wuttig, M., Magnetostriction of martensite. *Philos Mag A* **1998,** *77* (5), 1273-1299; (c) Lee, E. W., Magnetostriction and Magnetomechanical Effects. *Rep Prog Phys* **1955,** *18*, 184-229.

78.	Flanders, P. J., Impact-Induced Demagnetization, Magnetostriction and Coercive Force in Co-Doped Iron-Oxide Recording Tapes. *Ieee T Magn* **1976,** *12* (6), 770-772.

79.	Barandiaran, J. M.; Chernenko, V. A.; Gutierrez, J.; Orue, I.; Lazpita, P., Magnetostriction in the vicinity of structural transitions in Ni2MnGa. *Appl Phys Lett* **2012,** *100* (26).

80.   Aljiboory, M.; Lord, D. G., Study of the Magnetostrictive Distortion in Single-Crystal Terfenol-D by X-Ray-Diffraction. *Ieee T Magn* **1990,** *26* (5), 2583-2585.

81.   Gupta, A. K.; Gupta, M., Synthesis and surface engineering of iron oxide nanoparticles for biomedical applications. *Biomaterials* **2005,** *26* (18), 3995-4021.

82.   Skumiel, A., The effect of temperature on the anisotropy of ultrasound attenuation in a ferrofluid. *J Phys D Appl Phys* **2004,** *37* (22), 3073-3079.

83.   Jia, B. P.; Gao, L., Morphological transformation of Fe3O4 spherical aggregates from solid to hollow and their self-assembly under an external magnetic field. *J Phys Chem C* **2008,** *112* (3), 666-671.

84.   (a) Mendelev, V. S.; Ivanov, A. O., Ferrofluid aggregation in chains under the influence of a magnetic field. *Phys Rev E* **2004,** *70* (5); (b) Gazeau, F.; Dubois, E.; Bacri, J. C.; Boue, F.; Cebers, A.; Perzynski, R., Anisotropy of the structure factor of magnetic fluids under a field probed by small-angle neutron scattering. *Phys Rev E* **2002,** *65* (3).

85.   Kell, G. S., Density, Thermal Expansivity, and Compressibility of Liquid Water from 0 Degrees to 150 Degreesc - Correlations and Tables for Atmospheric-Pressure and Saturation Reviewed and Expressed on 1968 Temperature Scale. *J Chem Eng Data* **1975,** *20* (1), 97-105.

86.   Cao, Q. L.; Han, X. T.; Li, L., Numerical analysis of magnetic nanoparticle transport in microfluidic systems under the influence of permanent magnets. *J Phys D Appl Phys* **2012,** *45* (46).

87.   Lentacker, I.; De Cock, I.; Deckers, R.; De Smedt, S. C.; Moonen, C. T. W., Understanding ultrasound induced sonoporation: Definitions and underlying mechanisms. *Adv Drug Deliver Rev* **2014,** *72*, 49-64.

88.   Wood, A. K. W.; Sehgal, C. M., A Review of Low-Intensity Ultrasound for Cancer Therapy. *Ultrasound Med Biol* **2015,** *41* (4), 905-928.

89.   (a) Nappini, S.; Bombelli, F. B.; Bonini, M.; Norden, B.; Baglioni, P., Magnetoliposomes for controlled drug release in the presence of low-frequency magnetic field. *Soft Matter* **2010,** *6* (1), 154-162; (b) Podaru, G.; Ogden, S.; Baxter, A.; Shrestha, T.; Ren, S. Q.; Thapa, P.; Dani, R. K.; Wang, H. W.; Basel, M. T.; Prakash, P.; Bossmann, S. H.; Chikan, V., Pulsed Magnetic Field Induced Fast Drug Release from Magneto Liposomes via Ultrasound Generation. *J Phys Chem B* **2014,** *118* (40), 11715-11722; (c) Spera, R.; Apollonio, F.; Liberti, M.; Paffi, A.; Merla, C.; Pinto, R.; Petralito, S., Controllable release from high-transition temperature magnetoliposomes by low-level magnetic stimulation. *Colloid Surface B* **2015,** *131*, 136-140.

90.   Silva, S. M.; Tavallaie, R.; Sandiford, L.; Tilley, R. D.; Gooding, J. J., Gold coated magnetic nanoparticles: from preparation to surface modification for analytical and biomedical applications. *Chem Commun* **2016,** *52* (48), 7528-7540.